Received: 13 December 2018 | Accepted: 15 October 2019

DOI: 10.1002/jcp.29392

Journal of Cellular Physiology WILEY

ORIGINAL RESEARCH ARTICLE

Metabolic machinery encrypted in the Raman spectrum of influenza A virus-inoculated mammalian cells

Giuseppe Pezzotti[1,2,3,4] | Wenliang Zhu[1] | Tetsuya Adachi[4,5] | Satoshi Horiguchi[4,5] | Elia Marin[1,5] | Francesco Boschetto[1,4] | Eriko Ogitani[4] | Osam Mazda[4]

[1]Faculty of Materials Science and Engineering, Ceramic Physics Laboratory, Kyoto Institute of Technology, Kyoto, Japan

[2]Department of Orthopedic Surgery, Tokyo Medical University, Tokyo, Japan

[3]The Center for Advanced Medical Engineering and Informatics, Osaka University, Osaka, Japan

[4]Department of Immunology, Graduate School of Medical Science, Kyoto Prefectural University of Medicine, Kyoto, Japan

[5]Department of Dental Medicine, Graduate School of Medical Science, Kyoto Prefectural University of Medicine, Kyoto, Japan

Correspondence
Giuseppe Pezzotti, Ceramic Physics Laboratory, Kyoto Institute of Technology, Kyoto 606-8585, Japan.
Email: pezzotti@kit.ac.jp

Osam Mazda, Department of Immunology, Graduate School of Medical Science, Kyoto Prefectural University of Medicine, Kyoto 602-8566, Japan.
Email: omazda@gmail.com

Funding information
Ministry of Education, Culture, Sports, Science and Technology, Grant/Award Number: 17K01389; MEXT KAKENHI

Abstract

Raman spectroscopy was applied with a high spectral resolution to a structural study of Influenza (type A) virus before and after its inoculation into Madin–Darby canine kidney cells. This study exploits the fact that the major virus and cell constituents, namely DNA/RNA, lipid, and protein molecules, exhibit peculiar fingerprints in the Raman spectrum, which clearly differed between cells and viruses, as well as before and after virus inoculation into cells. These vibrational features, which allowed us to discuss viral assembly, membrane lipid evolution, and nucleoprotein interactions of the virus with the host cells, reflected the ability of the virus to alter host cells' pathways to enhance its replication efficiency. Upon comparing Raman signals from the host cells before and after virus inoculation, we were also able to discuss in detail cell metabolic reactions against the presence of the virus in terms of compositional variations of lipid species, the formation of fatty acids, dephosphorylation of high-energy adenosine triphosphate molecules, and enzymatic hydrolysis of the hemagglutinin glycoprotein.

KEYWORDS

Influenza virus, inoculation, MDCK cells, metabolic reactions, Raman spectroscopy, vibrational fingerprints

1 | INTRODUCTION

Among an increasingly complex and continuously improving scenario in biological analyses, Raman spectroscopy nowadays claims an authoritative position. Its recent spectacular awakening has brought it at the forefront of modern biochemical science (Baena & Lendl, 2004). In reviewing recent publications on biomolecules, it becomes clear how Raman spectroscopy has proved invaluable in unveiling a variety of issues in a number of key fields of microbiology, including metabolism of cells (M. Li, Romero-Gonzales, Banwart, & Huang, 2012; Notingher, 2007; Notingher, Verrier, Haque, Polak, & Hench, 2003; Smith, Wright, & Ashton, 2016), bacteria (Gonchukov, Sukhinina, Bakhmutov, & Minaeva, 2012; Lorenz, Wichmann, Stockel, Rosch, & Popp, 2017; Novelli-Rousseau et al., 2018; Strola et al., 2014), and viruses (Otange, Birech, Okonda, & Rop, 2017; Tuma & Thomas, 2002). The so far reported research also holds a promise for more accurate, fully quantitative, and rapid microbiological identifications of crucial issues in clinical diagnostics. However, the Raman investigators (including the present authors) have probably just scratched the surface in discovering the novelties this powerful spectroscopic method could bring.

One specific field of biology that could greatly benefit from the Raman spectroscopic method is certainly virology (Lambert, Whitman, Dyson, & Akula, 2006). The Raman probe could in principle

become a formidable diagnostic tool in virology, provided that methods of Raman virological assessments could be developed and made quantitative. However, Raman spectroscopy of viruses is yet in its infancy. In particular, the possibility of promptly distinguishing infected cells from healthy ones is particularly intriguing. One could exploit detailed spectral libraries for quickly locating cells infected by different types of viruses. Moreover, Raman analyses could give virologists a much clearer window at the molecular scale to study virus/cell interactions and to monitor in real-time the efficacy of antiviral treatments beyond the presently available analytical techniques. For example, it has long been known that viruses continuously evolve in the way they alter host cell pathways to enhance their replication efficiency (Chu, Dawson, & Elford, 1949; Sanchez & Lagunoff, 2015). Large-scale alterations in host cellular metabolism include aerobic glycolysis (or Warburg effect), fatty acid synthesis, glutaminolysis, and so forth. These are all modifications of carbon source utilization by infected cells that provide an enhancement in the available energy for virus replication and virion production, while temporarily elongating infected cell survivorship. The metabolic changes caused in cells are usually peculiar to each specific virus. Accordingly, clarifying the specific alterations promoting an enhanced viral replication might trigger the discovery of new therapeutic approaches, which exploit targeted inhibition of specific metabolic pathways in the host cells.

In this paper, we performed time-lapse Raman experiments on a model Madin–Darby canine kidney (MDCK) cell line with the purpose to study the infection of such cells by Influenza A virus. Influenza A virus is an enveloped virus of pleomorphic nature (i.e., long known to produce virions of both spherical and filamentous morphology; Chu et al., 1949; Sanchez & Lagunoff, 2015), which contains eight negative-sense RNA segments (SOIA Novel et al., 2009). Although this virus is usually only the causative agent of seasonal epidemics of respiratory illness, it has occasionally caused pandemics. In the most recent pandemic event (occurred in 2009; Palese & Shaw, 2007), the Influenza A virus was detected in approximately 200 countries, infected more than 600000 individuals, and was associated with approximately 8000 deaths (Maines et al., 2009). Further studies on this virus are needed to clarify its efficient transmission and to improve the yet limited availability of antiviral therapeutic options (Lynch & Walsh, 2007). Nowadays, vaccination is the best medical intervention available to protect humans against it (Nogales et al., 2014). With this background in mind, in vitro experiments using MDCK cells were selected here because this cell line was previously tested for vaccination purposes against Influenza A virus and its infection showed replication kinetics similar to that obtained upon infecting human cells (Nogales et al., 2014). The MDCK cell line was also indicated as a suitable choice for efficiently supporting replication and, thus, for correctly addressing the receptor binding preference of various viruses (Bradley et al., 2001; Gambaryan et al., 2005; Lugovtsev, Melnyk, & Weir, 2013). Different morphotypes of MDCK cells were shown to differ in a number of physiological properties, including intracellular pH and direction of ion transport and secretion (Ebner & Marin-Grez, 1998; Fernandez, Oliveira-Souza, & Malnic, 2000; Gekle, Wunsch, Oberleithner, & Silbernagl, 1994; Wunsch, Gekle, Kersting, Schuricht, & Oberleithner, 1995). Accordingly, certain variability was observed in supporting viral replication (Lugovtsev et al., 2013). Previous studies using such cells in combination with Influenza A virus (Buehler et al., 2013; Lugovtsev et al., 2013; Muramoto, Noda, Kawakami, Akkina, & Kawaoka, 2013) clarified many aspects of the replication events accomplished by virus proteins, but they also left some open questions about the mechanisms involved with energy consumption and protein translation. With the present Raman study, we hope to partly contribute to answering such yet obscure aspects of virus/cell interactions. In substance, the purpose of this study is three-fold:

(a) To accurately record the Raman spectra of both Influenza A virus and MDCK kidney cells as separate items with the high spectral resolution, to rigorously deconvoluting all the observed vibrational bands, and to label them according to their physical origin.
(b) To verify whether or not virus inoculated kidney cells could be clearly distinguished from clean cells.
(c) To record eventual fingerprints of altered metabolism as they appear in the Raman spectrum of infected kidney cells due to the incorporation of the virus in the endocytotic space.

To the authors' knowledge, this is the first time that an infective process is studied by a Raman approach with high spectral resolution and in time-lapse on living cells rather than through the use of specific fluorescent tags incompatible with cell life. We also believe that the proposed approach could have a general value in medicine, beyond this specific application.

2 | EXPERIMENTAL PROCEDURES

2.1 | MDCK cells and influenza A virus

The MDCK cells were obtained from the Riken cell bank (Ibaraki, Japan). The cells were preliminary suspended in a concentration of 1×10^6 cells/ml in Dulbecco's modified Eagle's medium (DMEM; Nacalai Tesque, Kyoto, Japan) supplemented with 10% fetal bovine serum, 100 U/ml penicillin, and 100 μg/ml streptomycin (Complete Medium), and seeded onto glass-based dishes (TECHNO GLASS Co., Shizuoka, Japan). Cells were then cultured in Complete Medium at 37°C in an atmosphere containing 5% CO_2.

The Influenza A virus (A/Puerto Rico/8/1934 H1N1 [PR8]) was kindly supplied by Dr. Hasegawa of the Influenza Virus Research Center, National Institute of Infectious Diseases. After washing the MDCK cells once, they were infected with Influenza A virus at a multiplicity of infection of 0.01 for 48–72 hr.

2.2 | Immunochemistry assays

To optimize the conditions of viral inoculation, several immunochemistry assays were preliminary applied. We visualized the MDCK cells before and after inoculation by the Influenza A virus in the fluorescence microscope after treating the cells with TBS (20 mM Tris-HCl pH 7.5, 150 mM NaCl), fixing them with 4%

paraformaldehyde for 10 min at room temperature, and finally washing with 0.1% Triton X in TBS. Successively, the cells were blocked with 2% skim milk in TBS for 60 min at room temperature, and stained with primary antibodies (Anti-influenza A Virus Nucleoprotein antibody; Abcam, Cambridge, UK) for 60 min at room temperature. After washing with a washing buffer, cells were incubated with an Alexa 594 Goat Anti-mouse IgG F(ab')2 (Thermo Fisher Scientific, MA) and Phalloidin Alexa 488 (Thermo Fisher Scientific) and 4′,6-diamidino-2-phenylindole (DAPI; Bacstain DAPI solution, Dojindo, Kumamoto, Japan) for 60 min at room temperature in the dark. The stained samples were then observed under a fluorescence microscope (BZX710; Keyence, Osaka, Japan).

Lactate dehydrogenase (LDH; Cytotoxicity Detection Kit Dojindo, Kumamoto, Japan), based on a colorimetric test for cell death, was applied to statistically quantify cell death. LDH is a stable cytoplasmic enzyme, which is present in all cells but is only released when the plasma membrane is damaged. In the cell death assay, LDH cytotoxicity was assessed on culture supernatants by measuring the absorbance at 490 nm on a plate reader (EMax, Molecular Devices, CA). Tests were repeated three times ($n = 3$) on each sample and statistics were performed according to the unpaired Student's *t*-test. A $p < .05$ was taken as statistically significant and labeled with one asterisk.

To perform the plaque assay, the MDCK cells were washed twice with PBS(−) and infected with PR8 at a multiplicity of infection of 0.01. After 1 hr adsorption, the remaining viruses were removed. The infected cells were incubated with DMEM containing 2.5 μg/ml trypsin (Sigma-Aldrich Co. LLC, Saint Louis) and 0.2% albumin (Wako Pure Chemical Industries, Ltd., Osaka, Japan) in a CO_2 incubator for 48–72 hr. The culture supernatants were harvested at 48 hr postinfection (hpi) and 72 hpi followed by centrifugation at 3,000 rpm, 4°C for 10 min. Virus titers of supernatants were assayed by the plaque method. A confluent monolayer of MDCK cells in a six-well plate was washed twice with serum-free DMEM (SF DMEM), followed by infection with 100 μl of virus suspension in a tenfold serial dilution. After incubation at 37°C for 1 hr with tilting every 10 min, the unabsorbed inoculum was removed, and infected cells were overlaid with 4 ml of agar DMEM (SF DMEM containing 0.8% agarose, 0.2% albumin, and 2.5 μg of trypsin per ml). The plate was incubated at 37°C in an atmosphere of 5% CO_2 for 2 days. For plaque counting, cells were fixed with a 5% glutaraldehyde solution for 2 hr, the agarose medium was then removed, and the cells were stained with 1% crystal violet.

2.3 | In situ Raman spectroscopy

In situ Raman spectra were collected on living cells using a highly sensitive instrument (LabRAM HR800, Horiba/Jobin-Yvon, Kyoto, Japan) operated with a 20× optical lens. The spectroscope was set in microscopic measurement mode with confocal imaging capability in two dimensions by means of a holographic notch filter incorporated into the optical circuit to achieve high spectral sensitivity. It allowed high-efficiency and high-resolution spectral acquisitions. The excitation source was set at 532 nm with a power of 10 mW. A spectral resolution better than 1 cm^{-1} could be achieved throughout the spectroscopic experiments by using an internal reference to calibrate the spectrometer at each measured spectrum. The Raman emission was monitored by a single monochromator connected with an air-cooled charge-coupled device (CCD) detector (Andor DV420-OE322; 1024 × 256 pixels). The acquisition time was fixed at 10 s. In time-lapse assessments, viruses, uninfected cells, and virus-inoculated cells were assessed in situ at increasing inoculation times (48 and 72 hr). The spectra used for analyses were averaged over 30 spectral collections at different locations per each sample and each inoculation time. Raman spectra were deconvoluted into Gaussian–Lorentzian sub-bands using a commercially available software package (LabSpec 4.02, Horiba/Jobin-Yvon). All spectra were discussed with respect to their relative intensity after normalization to the Symmetric ring-breathing mode in phenylalanine, which displayed at 1001 cm^{-1} in the spectra of both cells and viruses.

2.4 | Statistical analyses

The unpaired Student's *t*-test was utilized for statistical analyses. For a given sample size, *n*, a $p < .05$ was considered statistically significant and labeled with one asterisk. On the other hand, $p > .05$ was considered statistically insignificant and labeled "*n.s.*".

3 | EXPERIMENTAL RESULTS

3.1 | Fluorescence imaging of uninfected and infected cells

As a preliminary step in our spectroscopic investigation, we confirmed by fluorescence microscopy inoculation and intracellular localization of the Influenza A virus into MDCK cells. Figures 1a,b show fluorescence microscopy images of MDCK cells before and after 48 hr inoculation by Influenza A virus, respectively. The fluorescence micrograph in (a) shows only the green labels of F-actin and blue spots of nuclei, while (b) gives F-actin (stained green), nuclei (blue), and virus nucleoproteins (stained red). About 50% of the cell population exhibited NP localization in the cytoplasm, and the inoculation behavior was similar after 48 and 72 hr. This fraction is in good agreement with data reported by Chutiwitoonchai and Aida (Chutiwitoonchai & Aida, 2016) in a similar investigation. NP protein localized in the cytoplasm. However, it is known that viral NP protein is synthesized in the cytoplasm before being imported into the nucleus and then exported to the cytoplasm for further viral particle assembly and budding (Chutiwitoonchai & Aida, 2016).

The results of LDH cytotoxicity tests ($n = 3$) on MDCK cells after virus inoculation for 48 and 72 hr are shown as optical density (OD) values in Figure 1c. Since the stable cytoplasmic enzyme LDH is only released when the plasma membrane is damaged, the data shown in (c) represent the dependence on inoculation time of virus-induced damage on MDCK cells relative to cells before inoculation.

The plaque assay was applied in addition to the LDH cytotoxicity test because this assay is widely applied and assumed as the standard method in determining virus concentration in terms of infectious

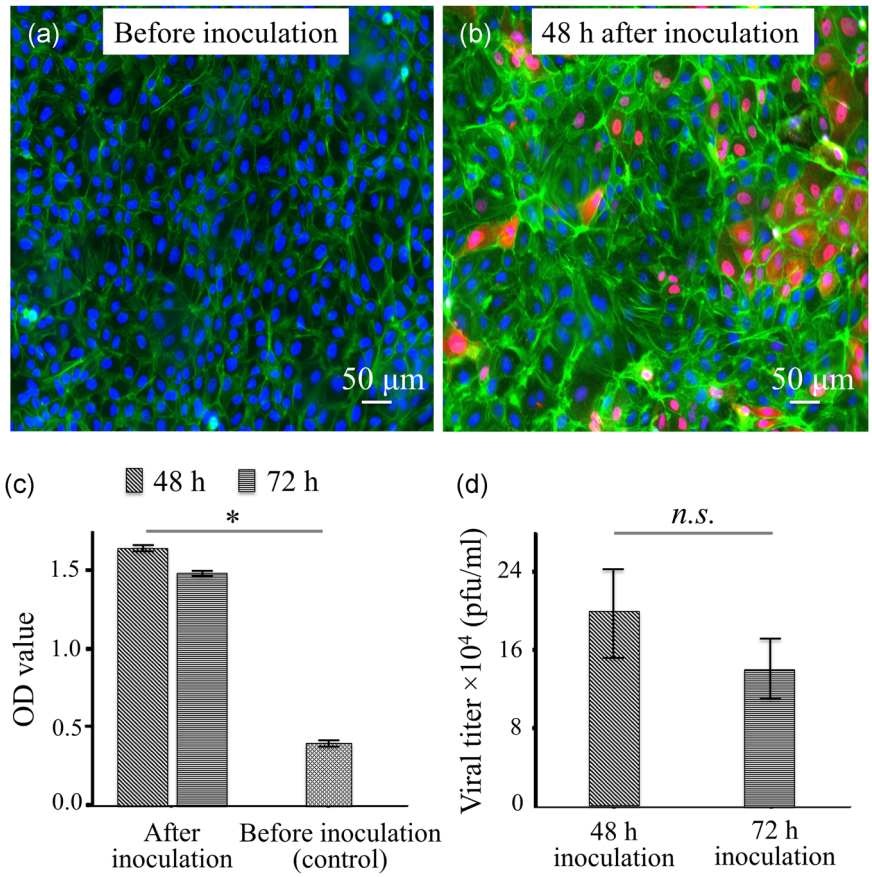

FIGURE 1 Fluorescence microscopy images of Madin–Darby canine kidney (MDCK) cells (a) before and (b) after 48 hr inoculation by Influenza A virus; F-actin, cells nuclei, and virus nucleoproteins stained green, blue, and red, respectively; in (c), results of lactate dehydrogenase cytotoxicity tests ($n = 3$) on MDCK cells after virus inoculation for 48 and 72 hr (the asterisk means that the difference is statistically significant $p < .05$); in (d), results of plaque assay are plotted as the number of plaque-forming units (pfu/ml) in cell samples as a function of viral inoculation time (48 and 72 hr; *n.s.* means statistically insignificant)

dose. We determined the number of plaque-forming units (pfu) in cell samples after 48 and 72 hr of viral inoculation and assessed virus quantity from pfu/ml counting under the assumption that each observed plaque represents one infective virus particle. Figure 1d shows the results of this experiment ($n = 3$). As seen, the infectious dose of virus concentration slightly differed at different times, but such difference was found to be statistically insignificant ($p > .05$ in Student's t test with $n = 3$).

The above-described fluorescence microscopy, LDH cytotoxicity test, and plaque assay results consistently demonstrate that, under the adopted experimental conditions, the virus successfully inoculated into and damaged the MDCK cells. Upon applying exactly the same experimental conditions for inoculation, we then performed a time-lapse Raman analysis on living cells before and after different times of viral inoculation, as described in the successive sections.

3.2 | Raman spectra of cells and virus before and after inoculation

Raman spectra were first collected over a wide spectral range between 550 and 1,850 cm^{-1} on separate samples of MDCK cells and Influenza A virus (Figure 2a,b). Then, spectra were collected in the same frequency interval after the inoculation of the virus into cells for 48 and 72 hr (Figure 3a,b). According to general classifications (Thomas, 1976a), the spectra were divided into three regions according to the main vibrational features that they contained, as follows: (a) the low-frequency C–S and C–C *backbone bond stretching region* (Zone I; 550–1000 cm^{-1}; cf. Figure 4); (b) the *ring-mode region* (Zone II; 1,000–1,400 cm^{-1}; cf. Figure 5); and, (c) the C═O (carbonyl) and C═C *double-bond region* (Zone III; 1,400–1,750 cm^{-1}; cf. Figure 6). In addition, a fourth zone referred to as the C–H *stretching region*, was recorded in the far high-frequency zone of the Raman spectrum (Zone IV; 2,800–3,100 cm^{-1}; cf. Figure 7). This latter zone will be discussed in a later section. Despite displaying some common vibrational characteristics, the Raman spectra of MDCK and Influenza A virus showed significant morphological differences (cf. different spectral zones in Figures 4–6a,b). Such differences were mainly related to the lack of DNA structure in the virus and to differences in proteins and lipids. This observation proves that it is possible to locate specific Raman fingerprints for cells and virus.

The spectra of virus-inoculated cells were different from that of cells before inoculation and strongly depended on inoculation time. Being affected by clear changes in the metabolism of both cells and viruses, the spectra after inoculation displayed morphologies far from the simple superposition of spectra from their individual constituents (cf. Figures 4–6c,d). This observation qualitatively proves that it is possible to clearly distinguish between clean and inoculated cells by analyzing their vibrational differences. A detailed description of the main differences in Zones I–III and their evolution with time after virus inoculation are given in the next three sections using highly spectrally resolved Raman acquisitions, and then normalizing and accurately deconvoluting the spectra into individual

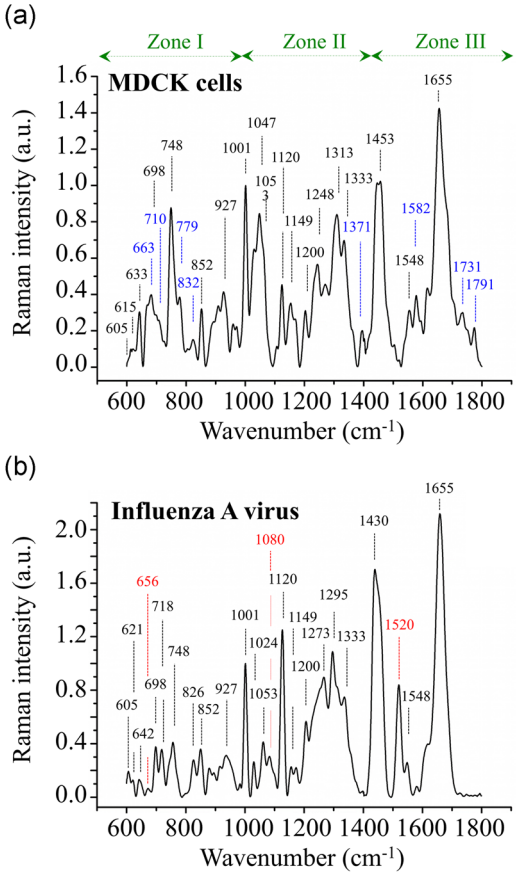

FIGURE 2 Raman spectra collected over a wide spectral range between 550 and 1850 cm^{-1}. (a) Madin–Darby canine kidney cells and (b) Influenza A virus. In blue and red colors are the bars only present in cells and virus, respectively

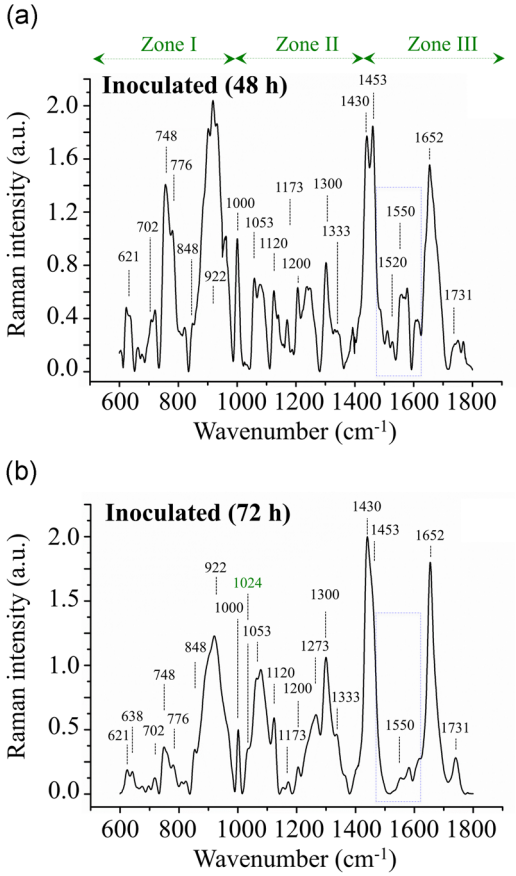

FIGURE 3 Raman spectra collected over a wide spectral range between 550 and 1850 cm^{-1} after the inoculation of the virus into cells for (a) 48 hr and (b) 72 hr. The blue box between 1500 and 1600 cm^{-1} represents a zone of significant metabolic changes and relates to C–N bonds

Gaussian-Lorentzian sub-band components (Figures 4–6 for Zones I, II, and III, respectively). Figure 7 shows the Raman spectra in the frequency zone between 2800 and 3100 cm^{-1} (Zone IV). Also in this high-frequency zone, which is dominated by C-H stretching, significant differences were observed between spectra collected from isolated cells and viruses as well as, after viral inoculation, at 48 and 72 hr. The trends observed at high frequencies will be discussed in a later section. The exact frequency values, the labels corresponding to those in Figures 4–7, the physical origin of all bands, and the related literature references are given in Tables 1–4, respectively.

3.3 | Highly resolved Raman spectra in the low frequency zone I

3.3.1 | Virus and cell spectra before inoculation

The following description of the Raman spectrum in the low frequency Zone I is based on band assignments as given in Table 1. Common to both cells and virus spectra, Bands 1 (at 606 cm^{-1}), 2 (at 621 cm^{-1}), and 3 (at 642 cm^{-1}) are related to ring stretching in cholesterol (Krafft, Neudert, Simat, & Salzer, 2005), C–C twisting in tyrosine/phenylalanine (Severcan, Akkas, Turker, & Yucel, 2012; Stone, Kendall, Smith, Crow, & Barr, 2004), and C–C twisting in tyrosine (Severcan et al., 2012; Stone et al., 2004), respectively. Three bands from DNA appear at low frequencies, which are only found in cells (emphasized in blue ink in Figure 4a and Table 1), viz.,: Bands 1+ (at 615 cm^{-1}), 4 (at 663 cm^{-1}), and 9 (at 710 cm^{-1}), which belong to ring bending in DNA cytosine (Otto, van den Tweel, de Mul, & Greve, 1986), C–S stretching in DNA cysteine (Otto et al., 1986), and ring breathing in DNA cytosine (Bankapur et al., 2012), respectively. An additional band only appearing in the cell spectrum in this zone is Band 2+ (at 633 cm^{-1}), which is assigned to out-of-plane C–O–H bending in glycerol (Krafft et al., 2005). The absence of Band 4 from C–S cysteine vibrations in the Raman spectrum of Influenza A virus is clearly related to a lack of DNA in the virus. However, the absence of vibrational signatures from the cysteine side chains that stem on the exterior of the capsid surface could be a consequence of low virus reactivity among different mutants (Wang, Lin, Johnson, & Finn, 2002). Conversely, two low-frequency bands were found only in the spectrum of virus (emphasized in red ink in Figure 4a and Table 1), viz., Bands 3+ (at 650 cm^{-1}) and 3++ (at 656 cm^{-1}). They both belong to C–S stretching in methionine (Podstawka, Ozaki, & Proniewicz, 2004; Zhu, Zhu, Fan, & Wan, 2011), which is the first standard amino acid at the N-terminal

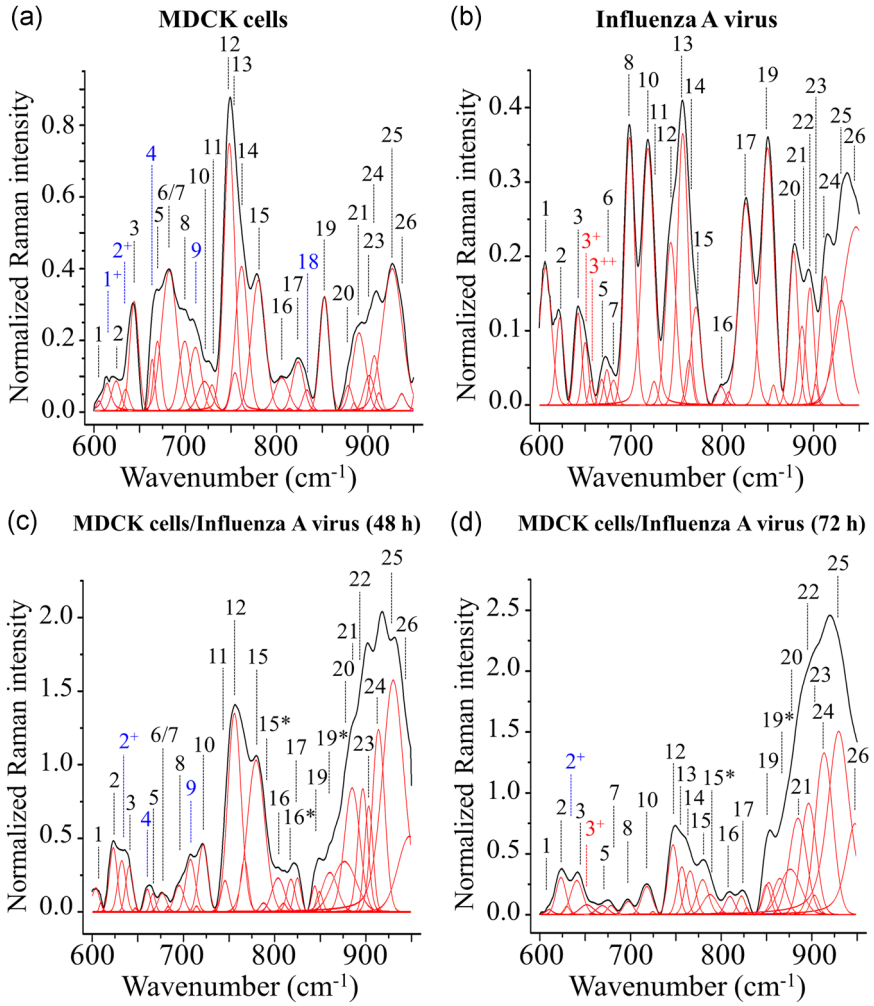

FIGURE 4 Highly resolved Raman spectra after normalization and deconvolution into Gaussian-Lorentzian sub-band components in the low-frequency Zone 1 (550~1000 cm^{-1}). The exact frequency values of the labeled bands are given in Table 1 together with the related literature references

position in virus hemagglutinin. Although Bands 3+ and 3++ are the only two C–S bands that appear in the virus spectrum, they are not the strongest emissions from C–S vibrations in methionine. Bands 8 and 10 (at 698 and 718 cm^{-1}, respectively) are also related to C–S stretching (CH_2 side). They represent the *gauche* and *trans* configurations of methionine, respectively (Podstawka et al., 2004; Xu & Lu, 2005; cf. Table 1). However, these bands greatly differed between cells and virus spectra, being significantly more intense in the latter spectrum. Signals from methionine will be further discussed in Section 4.1.

Bands 6 and 7 (at 675 and 681 cm^{-1}, respectively) appeared as a cumulatively (broad) singlet in the cell spectrum (Figure 4a,b; but they could be resolved as two separate bands in the virus spectrum). The former band in principle represents the overlap of vibrations from D-mannose (Cowcher et al., 2016) and C-S stretching in cysteine (Jess, Garces-Chavez, Riches, Herrington, & Dholakia, 2007; Smith & Dent, 2006). As stated above, however, the contribution of cysteine C–S stretching could be limited in the present virus strain. On the other hand, Band 7 arises from ring breathing in RNA guanine (Dovbeshko et al., 2002; Lopes, Marques, Valero, Tomkinson, & Batista de Carvalho, 2012). The rather weak intensity of the ring-breathing band of RNA guanine Band 7 in the virus spectrum could be interpreted as a reassortment of the avian segment into a human strain of the studied virus sample. Human viruses have a higher fraction of uracil/adenine in their genomes in contrast with avian viruses, which have a higher percentage of guanine/cytosine (Rabadan, Levine, & Robins, 2006). Although one or more segments in human strains likely come from avian viruses, the nucleotide composition continuously changes in human hosts. In support of such argument, a steady-state increase of uracil/adenine has indeed been reported over the last decades versus a decrease in guanine/cytosine residues for viral subtypes evolved in the human host (Rabadan et al., 2006).

The Raman spectra of cells and viruses commonly display strong bands from nucleic acid molecules. Single-stranded RNA molecules in virus are encapsulated into a relatively thick envelope mainly made of proteins (capsid). Such viral capsids contain several hundreds of protein subunits. Accordingly, the Raman spectra of the virus are expected to mainly contain bands characteristic of RNA and proteins. RNA covers a relatively small fraction (~12%) in weight of the virion (Thomas & Murphy, 1975); however, basic Raman experiments on solutions of equivalent molar concentrations have shown that the relative intensity of protein bands is three- to four-fold weaker than that of bands from nucleic acids (Cao, Liquier, & Taillandier, 1995). Band 12 at approximately 748 cm^{-1}, is contributed by ring breathing

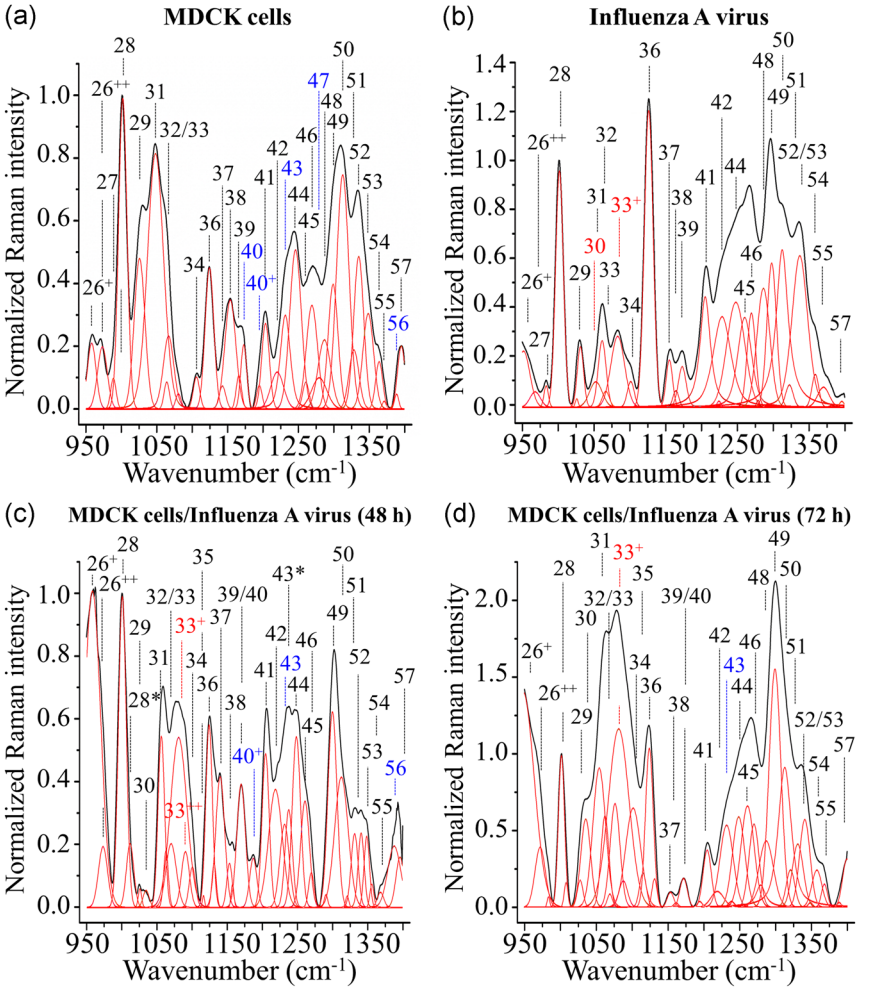

FIGURE 5 Highly resolved Raman spectra after normalization and deconvolution into Gaussian-Lorentzian sub-band components in the low-frequency Zone II (1000~1400 cm^{-1}); the exact frequency values of the labeled bands are given in Table 2 together with the related literature references

in both DNA and RNA (Dovbeshko et al., 2002), and it is the strongest feature in Zone I for the spectrum of MDCK cells, while it is clearly weaker in the spectrum of the virus due to the lack of DNA. Band 13 (at 756 cm^{-1}), which arises from ring breathing of tryptophan transient species (Huang et al., 2003; Johnson, Ludwig, & Asher, 1986), is the most preponderant signal in the spectrum of the virus. Tryptophan acts as a channel gate in Influenza A virus and is essential for acidifying the interior of virions during virus uncoating in the lumen of endosomes (Tang, Zaitseva, Lamb, & Pinto, 2002). This observation is also consistent with the relatively high intensity of Band 21 at 885 cm^{-1} (related to ring bending in tryptophan (Shetty, Kendall, Shepherd, Stone, & Barr, 2006)) in the virus spectrum as compared to that of cells (cf. Figure 4a,b). However, also D-Mannose strongly contributes to Band 21 as clearly located in Raman studies of different viruses by other authors (Xu & Lu, 2005). Note that Band 13 from transient tryptophan species is weaker in the spectrum of isolated cells as compared to the spectrum of the isolated virus. Vice versa, the tryptophan signal from proteins at 761 cm^{-1} (Band 14; Huang et al., 2003; Johnson et al., 1986) is stronger in cells than in viruses. Salzwedel, West, and Hunter (1999) reported an unusually high fraction of tryptophan residues in virus transmembrane and demonstrated the crucial role of a tryptophan-rich motif in enhancing efficiency in viral protease activity. In analogy with that study, we suggest that the intensity of Band 13 might testify the viral efficiency of the Influenza A virus. The three characteristics tryptophan Bands 13, 14, and 21 will be discussed in detail in Section 4.2.

The triplet at 826, 832, and 852 cm^{-1} (Bands 17, 18, and 19, respectively) arises from out-of-plane ring breathing in RNA/DNA (Notingher & Hench, 2006), ring breathing mode in tyrosine, and out-of-plane ring bending mode in tyrosine (H. M. Li, Wurrey, & Thomas, 1992; Yu, Jo, & O'Shea, 1973), respectively. While Band 18 is weak and only seen in the cell spectrum (cf. Figure 4a), the intensities of Bands 17 and 19 are quite strong in virus (cf. Figure 4b). The intensity ratio of Band 19 to Band 17, I_{852}/I_{826}, is sensitive to the nature of hydrogen bonds in the phenolic hydroxyl group and to its ionization, while it remains conspicuously insensitive to the environment of the phenyl ring and to the conformation of the amino acid backbone (Carey, 1982; Siamwiza et al., 1975). A low (~0.3), an intermediate (~1.25), and a high (~2.5) value for such intensity ratio mean a strong bond of the OH group with a negative acceptor, a moderately strong bond to H_2O, and bond of the OH group to a strong hydrogen bond acceptor, respectively. Values I_{852}/I_{826} approximately 1.5 were reported for the $-O^-$ form of the phenol side chain (Siamwiza et al., 1975). In other words, the phenolic oxygen is the acceptor atom in a strong H-bond for which the proton

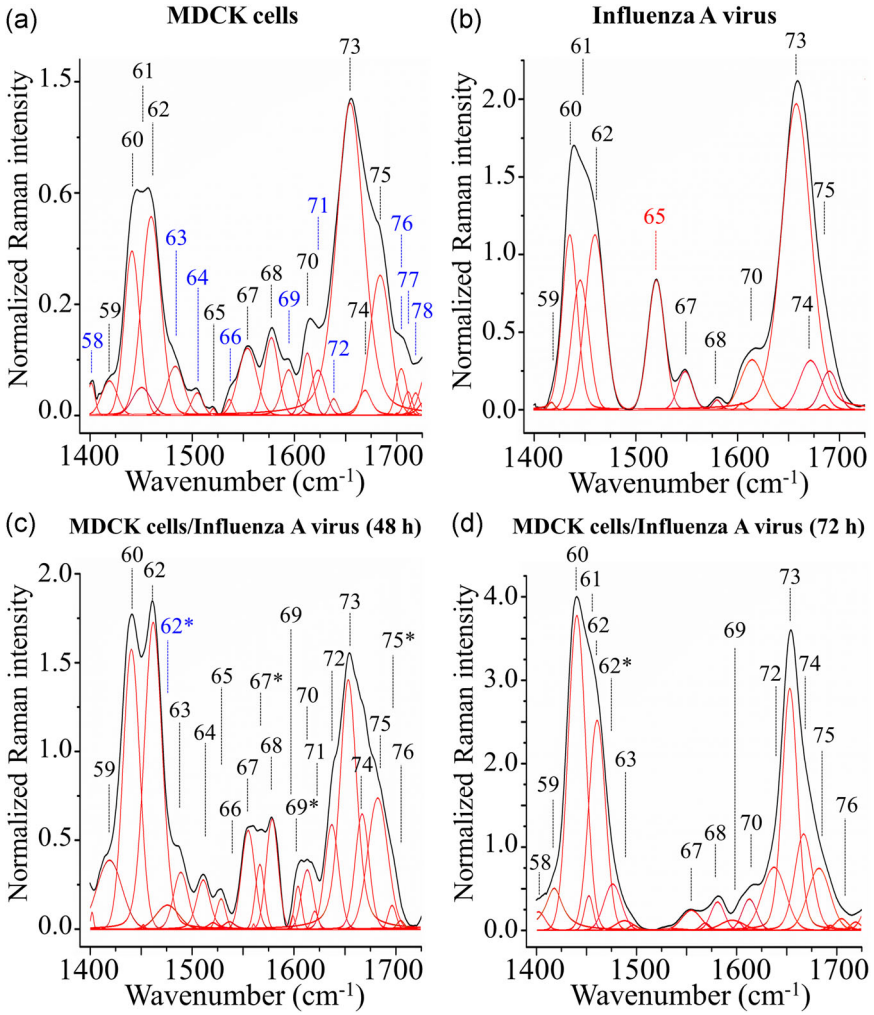

FIGURE 6 Highly resolved Raman spectra after normalization and deconvolution into Gaussian–Lorentzian sub-band components in the low-frequency Zone III (1400~1750 cm^{-1}); the exact frequency values of the labeled bands are given in Table 3 together with the related literature references

donor is very acidic hydrogen. This circumstance is also referred to as the existence of "buried" tyrosyl residues (Siamwiza et al., 1975), because these groups are trapped within protein structures in hydrophobic regions. On the contrary, at low I_{852}/I_{826} ratios, tyrosyl residues should be "exposed" to the protein surface because the state of the phenolic hydroxyl is that of a proton donor in a strong hydrogen bond to a very negative acceptor, such as a carboxylate ion. In Figure 4b, the ratio in the virus spectrum appears as an intermediate one (~1.27). While this yet confirms that tyrosine molecules are buried into protein structures, the recorded value of I_{852}/I_{826} ratio seems to be high for an isolated virus. Such a high value suggests that vibrations of different bonds could contribute to increasing the intensity of Band 19. Data in Figure 4b are thus in line with previous Raman studies of isolated virus (Xu & Lu, 2005), but the evolution of the I_{852}/I_{827} ratio with inoculation time supports the thesis of an additional vibrational contribution to Band 19 (i.e., from O–P–O stretching in adenosine triphosphate at 852 cm^{-1}; Bhaumik, Shearin, Delong, Wanekaya, & Ghosh, 2014; Rimai, Cole, Parsons, Hickmott, & Carew, 1969; as described later in Section 4.1).

Band 20 at approximately 877 cm^{-1} mainly arises from C–C stretching of hydroxyproline in proteins (Huang et al., 2003; Movasaghi, Rehman, & Rehman, 2007). Similarly, Bands 24, 25, and 26 at 915, 927, and 947 cm^{-1}, respectively, all represent C–C backbone stretching vibrations, which are extremely sensitive to protein conformation (Lord & Yu, 1970). Distinct differences could be observed between cell and virus spectra, indicating different bond fractions, mostly affected by divergences between cell proteins and envelop glycoproteins in the virus. All the remaining bands are labeled in the respective spectra and their physical origins indicated in Table 1.

3.3.2 | Spectra after virus inoculation into cells

Spectra in the frequency interval 600–650 cm^{-1}, as collected from inoculated samples after 48 and 72 hr (Figure 4(c) and (d), respectively) were compared with those collected on isolated cells and virus (Figure 4a,b). A clear variation could be located at approximately 633 cm^{-1} for the band labeled Band 2+. This band, which arises from C–O–H out-plane bending in glycerol (Krafft et al., 2005), is significantly more pronounced at 48 hr than at 72 hr inoculation time (cf. Figure 4c,d). The presence of the glycerol Band 2+ was also confirmed by the trend of the strongest glycerol signal at higher frequencies (i.e., at 1460 cm^{-1} Band 62 to be shown in a forthcoming section). Although in overlap with CH_2/CH_3 vibrations from proteins and other saccharides, Band 62 showed a

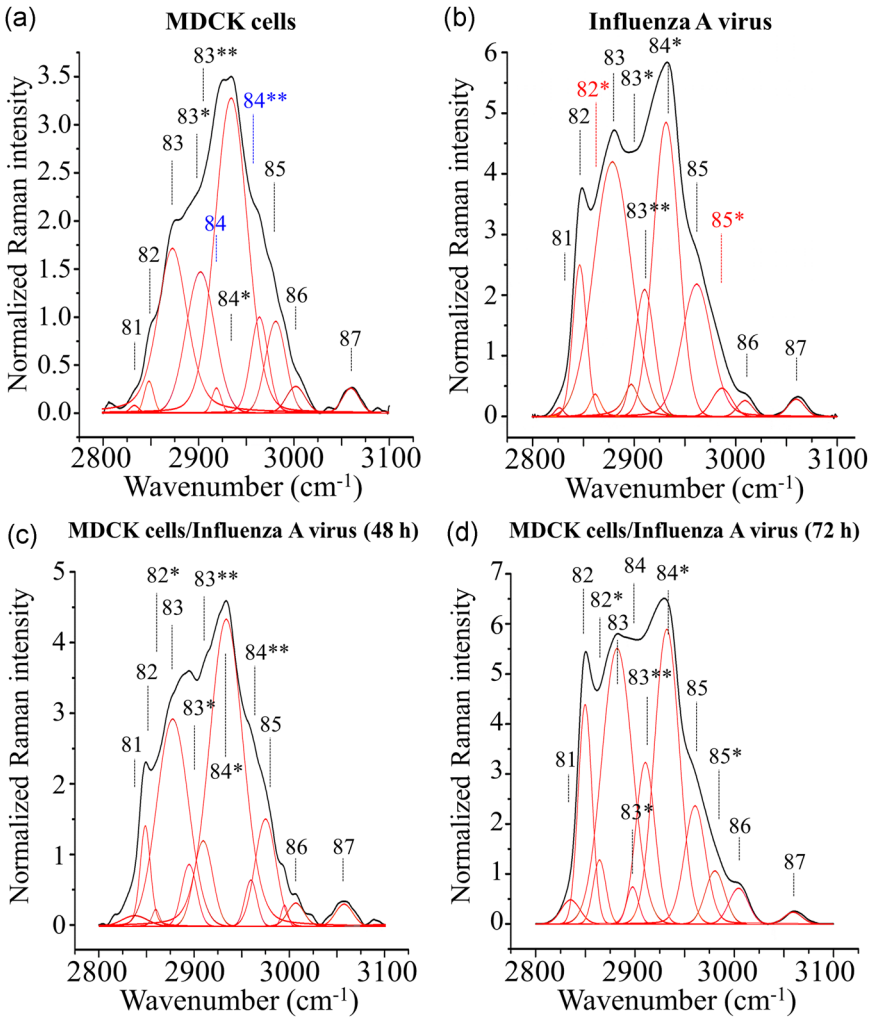

FIGURE 7 Highly resolved Raman spectra after normalization and deconvolution into Gaussian–Lorentzian sub-band components in the low-frequency Zone IV (2,800–3,100 cm^{-1}); the exact frequency values of the labeled bands are given in Table 4 together with the related literature references

trend after virus inoculation similar to that of Band 2+, namely a significant increase at 48 hr and a successive decrease at 72 hr after inoculation (cf. forthcoming Section 3.5). An enhanced presence of glycerol is conceivably related to the occurrence of enzymatic glycerol kinase, which is peculiar to the kidney (and liver) cells. The Raman data suggest that the presence of a virus initially stimulates the formation of glycerol to provide energy for cellular metabolism and to increase cell survivability. The cells, in reaction to viral inoculation, consume adenosine triphosphate to increase its energetic level. This is seen by a clear decrease of Band 19 (at ~852 cm^{-1}), which we assume to mainly represent O–P–O stretching in adenosine triphosphate (Rimai et al., 1969), while Bands 16* and 19* (at ~816 and ~865 cm^{-1}, respectively), which belong to O–P–O stretching in adenosine monophosphate and in mono/diphosphate molecules, respectively, newly appear at 48 hr after inoculation. Note that, in correspondence to the frequency of Band 12 (i.e., ~748 cm^{-1}), which we previously assigned to ring breathing vibrations in RNA/DNA, one could also expect a strong contribution from adenosine triphosphate, because this, is the strongest band found in the Raman spectrum of this molecule (Rimai et al., 1969). Indeed, the intensity of Band 12 conspicuously decreases after viral inoculation thus confirming the hypothesis of adenosine triphosphate consumption, although it is not possible to distinguish between the intensity contributions of different vibrational modes (cf. Table 1). A detailed discussion on the phenomenon of adenosine phosphate dephosphorylation will be given in the forthcoming Section 4.3.

In the Raman spectra after viral inoculation, additional fingerprints were found, which were consistent with variations in the lipid structure. It should be noted that variations in adenosine bands are conceivably related to variation in phospholipids through the machinery of energy transformation exploited by the virus after inoculation. This process will also be discussed in detail in Section 4.3 and a link is given with the trends of Bands 15 (at 779 cm^{-1}), 15* (at 789 cm^{-1}), and 23 (at 904 cm^{-1}), which are related to C–O–H out-of-plane bending in phosphatidylinositol, and O–P–O stretching in phosphatidylserine, respectively (Krafft et al., 2005; H. M. Li et al., 1992; Yu et al., 1973; cf. Table 1).

3.4 | Highly resolved Raman spectra in the intermediate frequency zone II

3.4.1 | Virus and cell spectra before inoculation

Zone II Raman spectra of MDCK cells and Influenza A virus are shown in Figure 5a,b. Table 2 describes all the Raman bands belonging to this zone with respect to their spectral locations and

TABLE 1 Labels, Raman frequencies, physical origins, and literature references of the deconvoluted bands in the low-frequency C–S and C–C *backbone bond-stretching region* (Zone I; 55–~1000 cm^{-1})

Band	cm^{-1}	Physical origin	Reference
1	606	Steroid ring stretching in cholesterol	Krafft et al. (2005)
1^{+}	615	Ring bending in DNA cytosine (only cells)	Otto et al. (1986)
2	621	C–C twisting in tyrosine and phenylalanine	Severcan et al. (2012); Stone et al. (2004)
2^{+}	633	Out-of-plane C–O–H bending in glycerol (only cells)	Krafft et al. (2005)
3	642	C–C twisting mode in tyrosine	Severcan et al. (2012); Stone et al. (2004)
3^{+}	650	C–S stretching in methionine (only virus)	Podstawka et al. (2004); Zhu et al. (2011)
3^{++}	656	C–S stretching in methionine (only virus)	Nishimura (1985); Podstawka et al. (2004)
4	663	C–S stretching in DNA cysteine (only cells)	Otto et al. (1986)
5	670	Ring breathing in RNA guanine	Chan et al. (2006); Williams and Edwards (1994)
6	675	Vibrations in D-mannose C–S stretching in cysteine	Cowcher et al. (2016); Jess et al. (2007); Smith and Dent (2006)
7	681	Ring breathing in RNA guanine	Dovbeshko et al. (2002); Lopes et al. (2012)
8	698	C–S stretching in methionine (CH_3 side; *gauche*)	Podstawka et al. (2004)
9	710	Ring breathing in DNA cytosine (only cells)	Bankapur et al. (2012)
10	718	C–S stretching in methionine (CH_3 side; *trans*)	Podstawka et al. (2004); Xu and Lu (2005)
11	725	C–N stretching in phosphatidylinositol Ring breathing mode in adenosine triphosphate	Chan et al. (2006); Krafft et al. (2005)
12	748	Ring breathing in RNA/DNA O–P–O stretching in adenosine triphosphate	Dovbeshko et al. (2002); Rimai et al. (1969)
13	756	Ring breathing of tryptophan transient species	Huang et al. (2003); Johnson et al. (1986)
14	761	Ring breathing of tryptophan in proteins	Huang et al. (2003); Johnson et al. (1986)
15	779	DNA phosphodiester stretching (only cells) C–O–H out-of-plane bending in phosphatidylinositol	Krafft et al. (2005); Williams and Edwards (1994)
15*	789	O–P–O stretching in phosphatidylserine	Krafft et al. (2005)
16	804	*N*-acetylglucosamine	She et al. (1974)
16*	816	O–P–O symm. stretching in adenosine monophosphate	Rimai et al. (1969)
17	826	Out-of-plane ring breathing in RNA/DNA	Notingher and Hench (2006)
18	832	Ring breathing mode in tyrosine (only cells)	Li et al. (1992); Yu et al. (1973)
19	852	Out-of-plane ring bending mode in tyrosine & O–P–O stretching in adenosine triphosphate	Bhaumik et al. (2014); H. M. Li et al. (1992); Rimai et al. (1969); Yu et al. (1973)
19*	865	O–P–O symm. stretching in adenosine monophosphate & diphosphate	Rimai et al. (1969)
20	877	C–C stretching of hydroxyproline in proteins	Huang et al. (2003)
21	885	Ring bending in tryptophan β-configuration in D-mannose (only virus)	Shetty et al. (2006); Xu and Lu (2005)
22	896	C–C backbone stretching	Chan et al. (2006)
23	904	Phosphatidylserine	Krafft et al. (2005)
24	915	C–C stretching in proline ring	Stone et al. (2004); Zhang et al. (2011)
25	927	C–C stretching in amino acids	Lau et al. (2003)
26	947	Skeletal modes in polysaccharides	Shetty et al. (2006)

physical origins. Band 28 at 1001 cm^{-1} represented the strongest emission in cells, which stemmed from symmetric ring breathing in phenylalanine (Stone et al., 2004, Stone, Kendall, Shepherd, Crow, & Barr, 2002). On the other hand, C–C stretching in fatty acids (De Gelder, De Gussem, Vandenabeele, & Moens, 2007; Band 36 at 1124 cm^{-1}) was the strongest emission observed in the virus spectrum in Zone II. This latter feature could be explained by considering that variations in the lipid composition of the viral envelope relate to virus infectivity and modulate viral fusion (Talari, Movasaghi, & Rehman, 2015). Free fatty acids are indeed known to promote positive curvature by introducing an inverted cone shape into the membrane and were abundantly found in the influenza virus

TABLE 2 Labels, Raman frequencies, physical origins, and literature references of the deconvoluted bands in the *ring-mode region* (Zone II; 1,000–1,400 cm^{-1})

Band	cm^{-1}	Physical origin	Reference
26^{+}	957	O–P–O symm. stretching in adenosine monophosphate	Rimai et al. (1969)
26^{++}	972	O–P–O symm. stretching in adenosine monophosphate	Rimai et al. (1969)
27	988	CH_3 rocking in tryptophan	Combs et al. (2005); Takeuchi et al. (1990)
28	1001	Symmetric ring breathing mode in phenylalanine	Stone et al. (2002); Stone et al. (2004)
28*	1011	Ring breathing in benzene ring of tryptophan	Combs et al. (2005); Takeuchi et al. (1990)
29	1025	C–C–H bending in benzene ring	Hernandez et al. (2013); Hernandez et al. (2016)
30	1035	C–C–H bending in ribose ring (only virus)	Hernandez et al. (2013); Hernandez et al. (2016)
31	1052	C–O & C–N stretching in proteins	Chan et al. (2006)
32	1063	C–C stretching in phospholipids	Krafft et al. (2005)
33	1066	N–C/C–C stretch & C–C–C bend phenol ring tyrosine	Hernandez et al. (2016)
33^{+}	1080	Guanine, adenine, and cytosine in RNA (only virus)	Xu and Lu (2005)
33^{++}	1090	O–P–Ostretching in adenosine diphosphate nucleoside	Jenkins et al. (1999)
34	1100	PO_2^- symm. stretching in RNA & phosphatidylinositol	Krafft et al. (2005); Ruokola et al. (2014)
35	1116	C–N stretching in protein	Xu and Lu (2005)
36	1124	Backbone C–C stretching in fatty acids, phosphatidylethanolamine and phosphatidylserine C–N stretching in D-mannose	De Gelder et al. (2007); Krafft et al. (2005); Xu and Lu (2005)
37	1142	NH_2 rocking in L-glutamate (cells) >C–O stretching in ribose residue of RNA (virus)	De Gelder et al. (2007); Hobro et al. (2007); Small and Peticolas (1971); Sumayya et al. (2008)
38	1155	CH_2 & NH_2 bending in L-alanine	Cory (2006); De Gelder et al. (2007)
39	1166	C=C stretching in lipids and C–C stretching in proteins	De Gelder et al. (2007); Kateinen et al. (2007)
40	1173	C–C–H bending in phenol ring in DNA (only cells)	Hernandez et al. (2016)
40^{+}	1195	Thymidine and cytosine in DNA (only cells)	Prescott, Steinmetz, and Thomas (1984)
41	1203	C–C stretching in phenol ring of phenylalanine	Hernandez et al. (2013); Hernandez et al. (2016)
42	1219	C–C stretching in the phenol ring of tyrosine	Hernandez et al. (2016)
43	1234	Amide III in β-sheet (only cells)	Iconomidou et al. (2001); Tuma and Thomas (2002)
43*	1239	NH_2 bending overlapping to Amide III in *N′*-formylkynurenine	Bieker and Schmidt (1979)
44	1247	NH_2 bending overlapping to Amide III in β-sheet Vibrations of *N*-formyl group in *N′*-formylkynurenine Amide III in random coil	Bieker and Schmidt (1979); Iconomidou et al. (2001); 2001; Lakshimi et al. (2002); Tuma and Thomas (2002)
45	1260	Out-of-plane ring bending mode in tyrosine	Hernandez et al. (2016)
46	1271	Amide III in random coil	Iconomidou et al. (2001)
47	1279	Amide III in α-helix (only in cells)	Ye, Li, Yang, and Luo (2014)
48	1286	CH_2 twist vibrations in fatty acids	De Gelder et al. (2007)
49	1299	CH_2 twisting/wagging in F glycoproteins Phosphatidylserine & phosphatidylethanolamine	Krafft et al. (2005); Lu et al. (2013)
50	1323	Amide III in α-helix of G glycoproteins	Lu et al. (2013)
51	1327	CH_3CH_2 wagging in purine bases of DNA Phospholipids	Viehoever, Anderson, Jansen, and Mahadevan-Jansen (2003) Malini et al. (2006)
52	1331	Ring stretching in adenosine triphosphate	D'Amico et al. (2015); Ochsenkühn et al. (2009)
53	1348	Amide III in N-formyl group Skeletal stretching in tryptophan benzene ring	Bieker and Schmidt (1979); Combs et al. (2005); Schmidt, and Bieker (1979); Takeuchi et al. (1990)
54	1357	Ring breathing in tryptophan	Johnson et al. (1986); Movasaghi et al. (2007)
55	1373	Ring breathing in thymine, adenosine, and guanine of DNA/RNA bases	D'Amico et al. (2015)
56	1388	Ring stretching & CH_3 bending in acetylthymidine	Lord and Yu (1970)
57	1398	C=O & CO_2^- symmetric stretching in L-glutamate	De Gelder et al. (2007); Faolain et al. (2005)

TABLE 3 Labels, Raman frequencies, physical origins, and literature references of the deconvoluted bands in the C═O (carbonyl) and C═C *double-bond region* (Zone III; 1,400–1,750 cm^{-1}). dGTP, dATP, and dCTP are abbreviations for deoxyguanosine, deoxyadenosine, and deoxycytidine triphosphates, respectively

Band	cm^{-1}	Physical origin	Reference
58	1402	Symmetric C═O stretching of COO^- (only cells)	Talari et al. (2015)
59	1419	C–H bending & C–N–C anti-symm. stretch in dGTP COO^- stretching in F glycoproteins	D'Amico et al. (2015); Lu et al. (2013)
60	1441	CH_2 scissoring in cholesterol & phosphatidylserine Acyl chains in sphingomyelin	Krafft et al. (2005); Malini et al. (2006)
61	1450	CH_2 scissoring in lipids & proteins	The et al., 2008
62	1460	CH_2/CH_3 deformation in proteins, glycerol & saccharides	Lu et al. (2013)
62*	1476	Adenine in DNA (B→A transition;only cells)	Peticolas (1995)
63	1483	C–N stretching in aromatic ring in dGTP/dATP (only cells)	D'Amico et al. (2015)
64	1505	C-N stretching mode in dATP (only cells)	D'Amico et al. (2015); Madzharova et al. (2016)
65	1521	C–N stretching in dTTP & ring stretching in dCTP (largely preponderant in virus)	Madzharova (2016); Thomas (1976a)
66	1529	C–N stretching in dGTP (only cells)	D'Amico et al. (2015); Madzharova et al. (2016)
67	1554	C═N stretching in dCTP	D'Amico et al. (2015); Madzharova et al. (2016)
67*	1568	C═N stretching in dATP & dGTP	D'Amico et al. (2015); Madzharova et al. (2016)
68	1578	C–C/C–N bending & CH_2 scissoring in dATP (only cells)	D'Amico et al. (2015)
69	1593	C(6)═N(1) stretching in dATP & dGTP (only cells)	D'Amico et al. (2015); Madzharova et al. (2016)
69*	1605	C–N stretching of *N*-formyl group in *N′*-formylkynurenine Ring vibrations in tyrosine	Bieker and Schmidt (1979); Lakshimi et al. (2002)
70	1614	C═C in tyrosine & tryptophan	Notingher et al. (2003)
71	1624	Aromatic ring stretching in dCTP (only cells)	D'Amico et al. (2015)
72	1639	C═O stretching & NH_2 scissoring in dCTP (only cells)	D'Amico et al. (2015)
73	1655	Amide I in α-helix	Tuma and Thomas (2002); Tuma (2005)
74	1669	Amide I in β-strand C═O stretching & N-H bending in sphingomyelin C═C stretching in cholesterol	Krafft et al. (2005); Tuma and Thomas (2002)
75	1684	Amide I in disordered structure	Shetty et al. (2006)
75*	1690	Amide I in turns & bands	Lakshimi et al. (2002)
76	1705	C═O stretching in dGTP & glutamic acid (only cells)	D'Amico et al. (2015); Madzharova et al. (2016); Shetty et al. (2006)
77	1711	C═O stretching in phosphatidylserine (only cells)	Krafft et al. (2005)
78	1719	C═O stretching in aspartic & glutamic acid (only cells)	Krafft et al. (2005); Shetty et al. (2006)

(Teh et al., 2008). As a confirmation of this interpretation, the virus spectrum in Figure 5b presents a prominent Raman signal at approximately 1286 cm^{-1} (Band 48), which arises from CH_2 twist vibrations in fatty acids (De Gelder et al., 2007). Band 48 is significantly less pronounced in the spectrum of isolated cells (cf. Figure 5a). Note also that both phosphatidylethanolamine and phosphatidylserine display strong emissions in correspondence of Band 36 (Krafft et al., 2005). Cone-shaped phosphatidylethanolamine facilitates membrane fluidity and provides the dynamics necessary for virus infection (Peticolas, 1995), while phosphatidylserine enhances virus entry through interaction with annexin proteins (Madzharova, Heiner, Gühlke, & Kneipp, 2016). Conversely, the strongest signal from phosphatidylinositol in this region (Band 49 at ~1300 cm^{-1}; Krafft et al., 2005) showed only a slightly higher intensity in the virus than in cells (cf. Figure 5a,b). The only Raman signal that displayed relatively strong in isolated virus but was conspicuously absent in isolated cells was the band labeled 33^+ at approximately 1,080 cm^{-1}. This band is in the region of C–N stretching for both protein and lipids, but it preponderantly represents guanine, adenine and cytosine residues in the RNA of viruses (Xu & Lu, 2005). While such spectral origin explains the observed strength in the present spectrum, it also suggests the possibility of Raman monitoring the level of virus inoculation in cells. A weaker marker of viral inoculation was seen as Band 30 at 1,035 cm^{-1} (ribose ring; Xu & Lu, 2005), but it only appeared as a shoulder to the stronger Band 31 at 1,052 cm^{-1} (cumulative C–O and C–N stretching in proteins; Chan et al., 2006). Spectra of cells after viral inoculation are discussed later in this section.

TABLE 4 Labels, Raman frequencies, physical origins, and literature references of the deconvoluted bands in the high-frequency C–H *stretching region* zone (Zone IV; 2,800–3,100 cm^{-1})

Band	cm^{-1}	Physical origin	Reference
81	2830	$(CH_2)_n$ symmetric stretching in lipids	Kolijenovic et al. (2005)
82	2849	CH_2 symmetric stretching in sphingomyelin	Krafft et al. (2005)
82*	2858	CH_2 symmetric stretching in lipids (only virus)	Kolijenovic et al. (2005)
83	2877	CH_3 symmetric stretching in lipids & proteins	Kolijenovic et al. (2005)
83*	2897	sp^3 C–H stretching in lipids & proteins	Lazar (2011)
83**	2912	CH band of lipids	Kline and Treado (1997)
84	2924	CH_2 antisymmetric stretching in lipids (only cells)	Kline and Treado (1997)
84*	2938	CH_2 antisymmetric stretching in lipids Chain end CH_3 symmetric band	Krafft et al. (2005)
84**	2965	CH_3 antisymmetric stretching in cholesterol/lipids (only cells)	Krafft et al. (2005)
85	2977	CH_3 antisymmetric stretching in lipids and fatty acids	Shetty et al. (2006)
85*	2984	Olefinic sp^2–CH_2 stretching (only virus)	Krafft et al. (2005)
86	3005	Unsaturated =CH stretching in lipids	Krafft et al. (2005)
87	3060	C–H in-plane stretching of phenyl rings	Cordero et al. (2013)

Conversely, several bands seen in the spectrum of isolated cells were missing in the spectrum of isolated virus (i.e., Bands 40, 40^+, 43, 47, and 56; emphasized in blue ink in Figure 5a and labeled in Table 2). All those fundamental spectral differences can be related to the absence of DNA in the virus and its different protein structures in comparison with cells. The stronger emission of Amide III for β-sheet and random coil structures (i.e., seen as the cumulative Band 43 at 1234 cm^{-1}; Iconomidou, Chryssikos, Gionis, Willis, & Hamodrakas, 2001; Tuma & Thomas, 2002) could not be resolved by our fitting algorithm in the spectrum of isolated virus. We assigned contributions from glutamate to both Bands 37 and 57 (at 1142 and 1398 cm^{-1}, respectively) according to literature (De Gelder et al., 2007; Faolain et al., 2005; Sumayya, Panicker, Tresa Varghese, & Harikumar, 2008). Glutamate is a nitrogen source utilized by the kidneys in various acid-base states for ammonia genesis (Thomas, 1976b). In kidney cells, biosynthetic pathways require the deamination of glutamine to glutamate to supply nitrogen for the nucleotides. As glutamine is utilized as a nitrogen source, nucleotide biosynthesis results in the production and accumulation of glutamate (Tuma, 2005). Glucose and glutamine are the primary sources of carbon utilized for energy homeostasis and biosynthesis (Yang et al., 2016). Viruses rely on host cellular metabolism to gain the energy required for their replication. Accordingly, they are not expected to show significant signals at the frequencies of Bands 37 and 57. The signal from Band 57 in Figure 5b is indeed negligible and the presence of Raman signals at the location of Band 37 can be explained by overlapping of C–O stretching in the ribose residue of RNA (Hobro, Rouhi, Blanch, & Conn, 2007; Small & Peticolas, 1971; cf. Table 2). Also peculiar to the cell spectrum, Band 56 at 1388 cm^{-1} has been assigned to acetyl-thymidine, as a byproduct of the thymidine kinase activity to encode virus-induced proteins (Lord & Yu, 1970).

3.4.2 | Spectra after virus inoculation into cells

As previously mentioned in describing the spectral Zone I (Figure 4c,d), spectral Zone II contains a clear fingerprint of a process of depletion in adenosine triphosphate due to hydrolysis of phosphoanhydride phosphate bonds that the cells employ in response to virus inoculation. In spectral Zone II after virus inoculation, the intensity of the main band of deoxyadenosine triphosphate (i.e., Band 52 at 1331 cm^{-1} in Table 2 and Figures 5c,d; D'Amico et al., 2015) showed a significant reduction at 48 hr and then remained stable at the same level at 72 hr after inoculation. Concurrently, Band 33^{++} at 1090 cm^{-1} appeared, which arises from O–P–O stretching in adenosine diphosphate (Jenkins, Tuma, Juuti, Bamford, & Thomas, 1999). In the same context, another quite striking feature was the strong enhancement of Band 26^+, which is related to O–P–O symmetric stretching in adenosine monophosphate (Rimai et al., 1969). These trends in Zone II are all consistent with the new appearance of Bands 16* and 19* in Zone I after viral inoculation (cf. Figure 4a,c), which are representative for O–P–O stretching in adenosine monophosphate and in both mono and diphosphate molecules, respectively (Rimai et al., 1969). Further discussion on triphosphate hydrolysis will be given in the forthcoming Section 4.3.

A further feature, which appears in comparing the Raman spectrum of virus-inoculated MDCK cells at 48 hr (Figure 5c) with the spectra of isolated cells and virus (in Figure 5a,b), is the presence of a new band (labeled Band 28* in Table 2) and emphasized in red ink in Figure 5(c). Band 28* at 1011 cm^{-1} is seen as a high-frequency shoulder of the strong phenylalanine Band 28 at 1001 cm^{-1} after 48 hr inoculation. It becomes a less distinct feature after 72 hr (Figure 5d). Band 28* is related to tryptophan residue (ring breathing (] Combs et al., 2005; Takeuchi, Nemoto, & Harada, 1990)). The enhancement of bands related to tryptophan at the expenses of cumulative DNA bands (e.g., Band 1^+, 4, and 9 in the low-frequency

Zone I) after viral inoculation will be discussed in Section 4.2 in the context of a metabolic reaction induced by the virus to create an internal state of disease tolerance in the cells (Scheiffele, Roth, & Simons, 1997). The spectral feature labeled as Bands 33^{+} (RNA-related) in the virus spectrum (Figure 5b) and lacking in the spectrum of isolated cells (Figure 5a) was found with enhanced intensity in the spectra of inoculated cells (Figure 5c,d). Conversely, Bands 29 and 50, related to DNA and proteins, were both found drastically reduced after 48 hr from viral inoculation, although they were partially restored after 72 hr. Such spectral variations clearly testify an increase in viral RNA at the expense of host cellular molecules and are in agreement with the observed reduction of deoxyadenosine triphosphate (i.e., Band 52) after viral inoculation. The clear trend inversion in the ratio between Bands 49 (mainly lipids) and 50 (mainly proteins) before and after virus inoculation (cf. Figure 5a,c) is also related to the exploitation by viruses of cellular (protein) molecules to form new lipids ones (phosphatidylinositol signaling in reaching internalization; Liu, Jia, Kelsey, Newland, & Mantsch, 2001) and phosphatidylserine membrane for macropinocytosis clearance of apoptotic debris (Henson, Bratton, & Fadok, 2001; Hoffmann et al., 2001; Ren & Savill, 1998; Savill, Fadok, Henson, & Haslett, 1993; Shiratsuchi, Kaido, Takizawa, & Nakanishi, 2000). This interpretation is consistent with the increase in the lipid signal as observed in Band 23 (phosphatidylserine) in Zone I after viral inoculation.

Bands 42 and 45 became quite strong after the inoculation of viruses in cells as compared to the original spectra of isolated cells and viruses (cf. Figure 5a–d). Both these bands are related to tyrosine (cf. Table 2). Following a recent study by Eierhoff, Hrincius, Rescher, Ludwig, and Ehrhardt, (2010), one of the strategies evolved by influenza viruses to penetrate the plasma membrane consists in abusing the signal-transduction machinery of the cells by binding to specific receptors (i.e., sialic acid residues) at the cellular surface. However, sialic acids do not function in transmitting signals across the plasma membrane and, as a signaling receptor, the virus exploits activating receptor tyrosine kinases. This peculiar signal-transduction machinery can thus explain the enrichment found in tyrosine-related bands during Influenza A virus inoculation into MDCK cells.

3.5 | Highly resolved Raman spectra in the high-frequency zone III

3.5.1 | Virus and cell spectra before inoculation

Figure 6a,b show the spectral Zone III in the C═O (carbonyl) and C═C double-bond *region* (1,400–1,750 cm^{-1}) for isolated MDCK cell and Influenza A virus samples, respectively. In Table 3, all bands found in this spectral zone are labeled according to literature (Bieker & Schmidt, 1979; D'Amico et al., 2015; Krafft et al., 2005; Lakshimi et al., 2002; Lu et al., 2013; Madzharova et al., 2016; Malini et al., 2006; Notingher et al., 2003; Peticolas, 1995; Shetty et al., 2006; Talari et al., 2015; Teh et al., 2008; Thomas, 1976a; Tuma, 2005; Tuma & Thomas, 2002). There were significant differences between the spectra of cells and virus also in this high-frequency zone. The most striking feature that differentiates the two spectra is the much lesser band population in the interval 1,470–1,625 cm^{-1} (8 bands labeled Bands 63~70 in the cells' spectrum vs. only 4 Bands 65, 67, 68, and 70 in the virus one). Additional bands seen in the cell spectrum but missing in the virus one were Bands 58, 71, 72, and 76–78. All bands missing in the virus spectrum are highlighted in blue ink in both Figure 6a and Table 3. The origins of a number of missing bands can be associated to elementary nucleotides, which are obviously missing in a single-strand RNA virus. On the contrary, Band 65 (centered at 1,521) was quite pronounced in the virus' spectrum and barely detectable in the cells' one. Raman emissions at around 1,520 cm^{-1} are related to C–N stretching in different RNA nucleosides (cf. Table 3). Accordingly, the observed spectral difference should be related to structural differences between the MDCK cells' DNA and the segmented negative-sense RNA of the Influenza A virus. Regarding the morphology of the Amide I bands from different protein secondary structures in the interval 1,653–1,692 cm^{-1}, there are two Bands clearly observed at 1,655 and 1,684 cm^{-1} (Bands 73 and 75; Figure 6a,b) in the spectra of both cells and viruses. However, the much weaker intensity of Band 75 in virus suggests a preponderance of α-helix above disordered configurations, while the cells were comprehensive (in different proportions) of all types of secondary structures. This difference might be related to the peculiar presence of hemagglutinin proteins at the virus surface, whose binding sites consist of α-helices and loops (Yang et al., 2016). The Raman Band 74 overlaps vibrations from β-strands and lipids (cf. Table 3), in which individual contributions could not be resolved. Viruses belonging to the influenza viral family have indeed been shown to be high in cholesterol and sphingomyelin (Scheiffele et al., 1997). Both these lipids present relatively strong Raman bands at approximately 1,670 cm^{-1} (Krafft et al., 2005). Accordingly, lipids could also contribute to Band 74, as observed in the virus spectrum of Figure 6b. Note also that the strongest Raman bands of cholesterol and sphingomyelin appear at 1,440 and 1,437 cm^{-1}, respectively (Krafft et al., 2005). As a matter of fact, we can also observe a strong intensity for Band 60 in the virus spectrum, whose maximum lies at around that frequency.

3.5.2 | Spectra after virus inoculation into cells

The production of glycerol after virus inoculation, which was mentioned in the context of Zone I (Figure 4(c) and (b)), could partly be confirmed in Zone III upon monitoring the trend of the strongest Raman band of glycerol at 1460 cm^{-1} (Band 62; cf. Figure 6c,d, and Table 3). This band, which arises from CH_2/CH_3 vibrations from both proteins and saccharides, showed a trend after virus inoculation similar to that of Band 2+, namely a significant increase at 48 hr and a successive decrease at 72 hr after inoculation. These variations are believed to represent fluctuations in glycerol concentration that follow metabolic adjustments of the cells in the presence of the virus.

The spectra of virus-inoculated cells at 48 and 72 hr (in Figure 6c,d) additionally showed two main differences as compared to spectra from isolated cells and virus, as follows:

(i) A new band, labeled as Band 69* appeared with a frequency at a maximum of 1,604 cm^{-1} (cf. Table 3).
(ii) Bands 64–66, included in the frequency interval between 1,500 and 1,550 cm^{-1}, disappeared from the spectrum of inoculated cells after 72 hr after an initial increase at 48 hr (cf. Figure 6c,d).

Regarding the above item (a), such newly observed emission has also been related to ring vibrations in tyrosine and it was shown strongly enhanced in oxidized deoxyguanosine triphosphate (D'Amico et al., 2015; Lakshimi et al., 2002; Thomas, 1976a). This interpretation is supported by the observed intensity enhancement for Bands 42 and 45, which was discussed in the previous section as a fingerprint of tyrosine kinase activation upon virus inoculation (Eierhoff et al., 2010; cf. Figure 5 and Table 2). On the other hand, the above item (b) can be the consequence of damages to the cells' DNA structure upon viral attack, which is seen as an intensity reduction of DNA-related bands in the Raman signals from cells (cf. also intensity reduction for Band 63).

3.6 | C–H stretching zone IV

The Raman spectra collected from isolated MDCK cells and Influenza A virus in the high-frequency Zone IV showed significant morphological differences between each other (cf. Figure 7a,b). However, both spectra displayed bands related to CH_2 and CH_3 vibrations, and of common origin for lipids and proteins (cf. Table 4; Cordero et al., 2013; Kline & Treado, 1997; Kolijenovic, Scut, Vincent, Kros, & Puppels, 2005; Krafft et al., 2005; Lazar, 2011; Shetty et al., 2006). One main difference resided in Band 82 (at 2,849 cm^{-1}) being significantly less pronounced in virus than in cells. This spectral characteristic indicates a stronger contribution from sphingomyelin in the virus spectrum. This interpretation is supported by the relatively stronger intensity of Band 74 (at 1,669 cm^{-1}) described in Table 3 as an Amide I-like vibrations from sphingolipids (Krafft et al., 2005; cf. Figure 6b). Conversely, Band 84** located at 2,965 cm^{-1} was only present in the cells' spectrum and testifies a higher contribution from cholesterol molecules. Regarding spectra after virus inoculation into cells (cf. Figure 7c,d), the main evolution was the increase of Band 83 (at 2,877 cm^{-1}), clearly seen at 48 hr and then becoming more pronounced after 72 hr. This variation is however of difficult interpretation because Band 83 represents a Raman emission cumulative of CH_3 bonds from both lipids and proteins.

4 | DISCUSSION

We here attempt to interpret the Raman results according to general notions of virology and cell physiology. When the virus penetrates the host cells, it efficiently succeeds in exploiting cell energy, synthetic machinery, and low molecular weight precursors to promote its viral replication. The standpoint here is that a successful Raman analysis of virus inoculation should be able to retrieve meaningful hints about elementary processes of viral inoculation and replication. It should be noted at the outset that our interpretation unavoidably lacks completeness due to the complexity of the phenomena observed. However, some important aspects of the metabolic machinery could clearly be caught by the Raman probe. Those aspects represent at the molecular level how the viral population actually penetrates the cell membrane and develops internally. We show here that biophysical reactions are indeed encrypted in the Raman spectrum and their spectroscopic interpretation could be useful to quantify the viral invasiveness and its progressive development. For example, one could monitor in time-lapse the intensity of the DNA bands from the cells and judge about the rate of DNA synthesis in the cells. An additional option could be to monitor intensity and frequency variations of bands related to methionine, which assists the translation of messenger RNA in viral hemagglutinin, and whose intensity increase and frequency shift directly relates to the degree of virulence, as explained in the following sub-section.

4.1 | Viral obstruction to cell metabolism and hemagglutinin unfolding

RNA viruses can be classified according to their modes of replication, with RNA polarity playing a fundamental role in determining the replicative mechanism. Influenza A virus is a single-stranded, negative-sense (or minus-strand), segmented RNA virus (Palese, Zheng, Engelhardt, Pleschka, & Garcia-Sastre, 1996). Accordingly, it does not directly translate its RNA into protein but preliminary carries an RNA polymerase inside the virion (Bouvier & Palese, 2008). During the process of viral replication that follows cell penetration, the virus starts to dismantle and to inject its genetic material into the cell cytoplasm. Multiple segments of single-stranded negative-sense RNA are bonded with heterotrimeric viral RNA-dependent RNA polymerase and multiple copies of nucleoprotein to form viral ribonucleoprotein complexes. Transcription of viral genes and replication of the viral RNA genome take place within such complexes (Te Velthuis & Fodor, 2016). In the case of Influenza A virus, the way polymerase copies the RNA template in the context of ribonucleoprotein complexes has not yet been fully clarified. However, it has been established that viral RNA first enters the nucleus to serve as a template to synthesize messenger RNA (mRNA). This process takes place with polymerase pulling the template viral RNA from the oligomeric nucleoprotein helix at the nucleus entry channel into its active site (Te Velthuis & Fodor, 2016). mRNA is then transported from the nucleus back to the cytoplasm to produce a full-length plus-strand, which is then copied into a full-length minus-strand RNA to be employed in assembling new virions. This model is compatible with the "chemical" view that template viral RNA progressively dissociates from nucleoproteins, then is transferred into the polymerase active site, and finally re-associates with nucleoproteins (Te Velthuis & Fodor, 2016). As part of the process of viral mRNA synthesis, Influenza A virus inhibits macromolecular synthesis in the host cell to provide an advantage for the synthesis of virus proteins and nucleic acids in the absence of competing for synthesis of cellular products. The influenza virus also shares with

herpes simplex virus an attitude to impede cellular mRNA binding with ribosomes to form polyribosomes. In this way, only virus-specific mRNA remains allowed to bond, which gives viral mRNAs a selective advantage. Cell DNA synthesis is also inhibited by decreasing cellular protein synthesis. The challenge here is whether one could discern fingerprints of such elementary processes upon in situ time-lapse Raman experiments.

The frequency interval 650–700 cm^{-1} in Zone I of the Raman spectra is dominated by RNA and DNA bands. Noticeably, in this study, it was possible to distinguish between RNA and DNA contributions upon comparing the pristine Raman spectra of individual cells and virus before inoculation (Figure 4a,b), because the latter lacks DNA. Moreover, upon recording the Zone I spectrum on virus-inoculated cells (Figure 4c,d), we could clearly observe some biochemical changes that virus operates on cells' DNA/RNA. Band 7 (at 681 cm^{-1}) is a peculiar fingerprint of ring breathing modes of the nitrogenous guanine base in RNA (Dovbeshko et al., 2002; Lopes et al., 2012). This band is stronger in the cell spectrum than in the virus one, but it could not be separated from the neighboring Band 6 related to C–S stretching in cysteine (Jess et al., 2007; Smith & Dent, 2006; cf. Figure 4a,b and Table 1). On the other hand, Bands 4 (C–S stretching in DNA cysteine at 663 cm^{-1}), 9 (ring breathing in DNA cytosine at 710 cm^{-1}), and 18 (ring breathing mode in DNA tyrosine at 832 cm^{-1}) relate to the DNA structure only and are absent in the pristine spectrum of virus (Bankapur et al., 2012; H. M. Li et al., 1992; Otto et al., 1986; Yu et al., 1973). Band 15 (at 779 cm^{-1}) arises from DNA phosphodiester stretching, a contribution that should thus be lacking in the virus spectrum (Williams & Edwards, 1994). However, this band appears in the spectrum of isolated virus because it also includes an overlap of C–O–H out-of-plane signals from phosphatidylinositol (cf. Table 1 (Krafft et al., 2005)). The vibrations of this lipid, which also appear at 725 cm^{-1} (Band 11; cf. Table 1; Krafft et al., 2005), influence the Raman spectrum of cells after viral inoculation, as separately discussed later in this paper.

The fact that Bands 4, 6, 9, and 18 conspicuously decrease in intensity after virus inoculation shows how Influenza A virus heavily obstructs any competing DNA synthesis in the cells to favor its own production of viral RNA templates, their successive transformation, and their assembling into new virions. In other words, a fingerprint of viral obstruction to cell metabolism can be found in the Raman spectrum of virus-inoculated cells upon monitoring the decrease in relative intensity of DNA-related bands.

Band 16 (at 804 cm^{-1}) is a relatively weak band present in the spectra of both cells and viruses (cf. Figure 4a,b). However, this band is important because it represents the only signal in the low-frequency interval of the monosaccharide *N*-acetylglucosamine. In other words, it can be considered to be a fingerprint for amino acid molecules (She, Dinh, & Tu, 1974). *N*-Acetylglucosamine is an amide derivative of glucose, which covers an important role in virology. Its presence is commonly explained according to the abundance of *N*-linked oligosaccharides covering the virion surface and, more specifically, to the fact that *N*-acetylglucosamine is the main component in the biosynthesis of hemagglutinin side chains in the Influenza A virus (Keil, Geyer, Niemann, Dabrowski, & Klenk, 1984). The detection of *N*-acetylglucosamine in the virus spectrum is a marker for the biosynthesis of hemagglutinin (i.e., the major surface protein of the influenza A virus). Methionine is, in turn, the first standard amino acid to be incorporated into the N-terminal position of all proteins and, in virus, mainly in hemagglutinin. In viral hemagglutinin, methionine assists the translation of messenger RNA. There are two different configurations (*trans* and *gauche*; cf. Figure 8a) for the methionine molecule and their C-S bond vibrations give important contributions to the Raman spectrum at low frequencies (Bands 8 and 10 at 698 and 718 cm^{-1}, respectively; cf. Table 1). Band 8 arises from C–S stretching at the methionine S–CH_3 side in *gauche* configuration (Chan et al., 2006; Cowcher et al., 2016; Podstawka et al., 2004; Williams & Edwards, 1994). This band is found in the pristine spectra of both cells and virus. Band 10 arises instead from C–S stretching at the methionine S–CH_3 side in *trans* configurations (Podstawka et al., 2004; Xu & Lu, 2005; Zhu et al., 2011). Note that Bands 8 and 10 are present in the pristine spectra of both cells and virus, but are significantly stronger in the virus spectrum, as expected according to the preponderant presence of hemagglutinin on the virus surface. We note for completeness that also Bands 3+ and 3++ are related to C–S stretching in methionine and only present in the virus spectrum. However, those latter bands are significantly weaker and are difficult to deconvolute from the neighboring Band 3 (cf. Figure 4b).

To properly interpret the intensity trend of Bands 3+, 3++, 8, and 10 before and after the viral attack, we need to consider the process of virus inoculation and the chemical events occurring during such process. When the virus enters in contact with the cell membrane, hemagglutinin binds to monosaccharide sialic acid and, through such a bond it sticks onto the cell surface. The cell then reacts by engulfing the virus into a membrane-bound compartment, which eventually separates to form an isolated (intracellular) volume referred to as endosome and containing the virus. Successive attempts by the cell to digest the endosome content mainly involve internal acidification of the endosome and its transformation into a lysosome capable of enzymatic hydrolysis. As soon as the internal pH drops down to approximately 6.0, the originally folded structure of the hemagglutinin molecule becomes unstable, partially unfold, and release a previously hidden portion of its peptide chain with hydrophobic characteristics. The acidic pH inside the vesicles also triggers a major structural transition of hemagglutinin leading to a new structure more stable at low pH and capable to chemically join the viral envelope of the endosomal membrane. In other words, hemagglutinin is essential to the entry process but unfolds and loses its structure after incorporation in endosomes. This process clearly explains why Bands 8 and 10, originally very strong in the isolated virus (cf. Figure 4b), tend to disappear after virus inoculation. Successive refolding liberates the viral genome and allows the virus pouring its RNA genome into the cell cytoplasm (Stegmann, Booy, & Wilschut, 1987).

As described in Section 3.3, the intensity ratio of the doublet at 826 and 852 cm^{-1} (Bands 17 and 19, respectively) was reported to be sensitive to the nature of hydrogen bonding in the phenolic hydroxyl

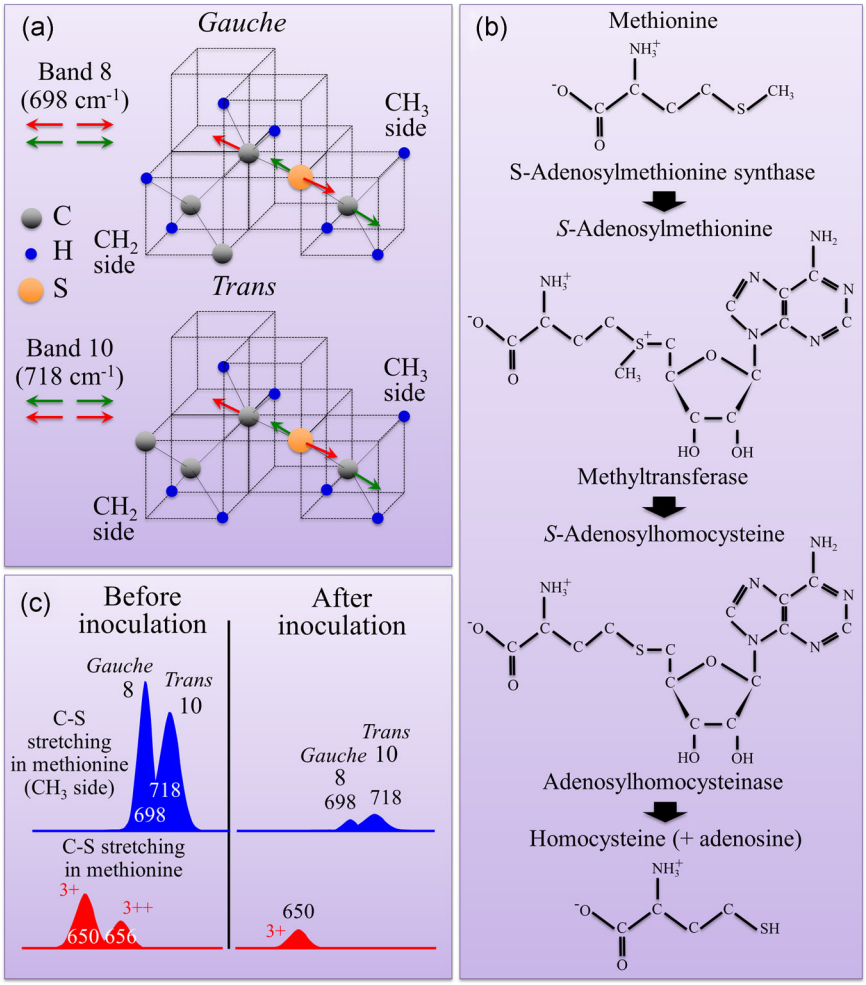

FIGURE 8 (a) *Trans* and *gauche* configurations of the methionine molecule and their characteristic C–S bond vibrations; (b) synthetic pathway after virus inoculation into cells showing reaction between methionine and adenosine triphosphate to form *S*-adenosylmethionine in endosomal acidic environment, successive rinsing off of the methyl group, and final cleavage to form homocysteine and adenosine; and, (c) schematic draft of the spectroscopic variations of Raman bands related to C–S bonds in methionine

group and to its ionization, while remaining insensitive to the environment of the phenyl ring and to the conformation of the amino acid backbone (Carey, 1982; H. M. Li et al., 1992; Siamwiza et al., 1975; Yu et al., 1973). Siamwiza et al., (1975) proposed to exploit this spectroscopic circumstance to distinguish between "buried" and "exposed" tyrosyl residues, thus spectroscopically distinguishing the stage of early inoculation from that of endosomal incorporation (i.e., in a low pH environment). However, in the present study of MDCK cells, we found it difficult to unequivocally deconvolute Bands 17 and 19 mainly due to the strong overlap of Band 19 with O–P–O stretching vibrations. An alternative possibility is newly proposed here, which exploits the results of a basic Raman study (Podstawka et al., 2004) on methionine-containing dipeptides as a function of environmental pH.

Upon virus inoculation into cells, methionine reacts with adenosine triphosphate in an endosomal acidic solution to form *S*-adenosylmethionine. In a successive reaction, the methyl group is removed by methyltransferase (e.g., by cytosine), and then hydrolysis cleaves the C–S bond (adenosylhomocysteinase) to form homocysteine and adenosine. Figure 8b shows a schematic draft of the above-described synthetic pathway. Following the removal of the CH_3 groups in acidic environment, the vibrational response of methionine is altered, and Bands 8 and 10 from virus hemagglutinin lose a significant amount of their strength, as we observed in our experiments. Figure 8c schematically shows the spectroscopic variations of Bands 8 and 10 (and of Bands 3+ and 3++ of similar origin) after viral inoculation. We thus propose to use the relative intensity of Bands 8 and 10 to monitor the alteration of methionine structure in viral hemagglutinin after virus engulfment in and environmental acidification of endosomes. Note finally that the existence of two different *trans* and *gauche* configurations for the methionine molecule involves different constants for the reaction with adenosine triphosphate, as well as different Raman cross-sections for the S–CH_3 vibrational moieties. This explains why the observed rate of decrease upon inoculation time is different for Bands 8 and 10 (i.e., Band 8 decreases faster than Band 10).

4.2 | Status of disease tolerance and the role of tryptophan

The amino acid tryptophan contains a peculiarity in its molecular structure: the indole ring functional group. Its stereoisomers, which share such a structural peculiarity, serve in a number of functions, including protein synthesis and generation of precursor molecules in various immunological pathways. Importantly in viral contexts, they anchor proteins within the cell membrane (De Jesus & Allen, 2013).

Tryptophan and its catabolites possess immunosuppressive functions and improve disease tolerance acting as key regulators in viral infections (Mellor & Munn, 2003). From a spectroscopic viewpoint, a straight consequence of the peculiar structure of the indole ring are some of its vibrational modes at frequencies isolated from those of other amino acids or molecular species in cell structures. By exploiting this fortunate circumstance, we shall attempt here to mark some peculiar aspects of disease tolerance in MDCK cells affected by virus following the trend of indole ring vibrations. Eight vibrational modes were reported for the indole ring of tryptophan (Takeuchi & Harada, 1986), which were classified into five in-plane and three out-of-plane modes. Of these eight modes, three bands are located in Zone I: Bands 13, 14, and 21 at 756, 761, and 885 cm^{-1}, respectively (Huang et al., 2003; Johnson et al., 1986); and two additional bands in Zone II (Bands 53 and 54 at 1348 and 1357 cm^{-1}). However, the signal of Bands 21 is preponderantly affected by contributions from the β-configuration of D-mannose (Xu & Lu, 2005), which impedes a clear separation from the tryptophan emission. Accordingly, we shall mainly discuss nonoverlapping signals from tryptophan ring breathing, namely Bands 13, 14, and 54. These selected vibrational modes are shown in Figure 8a. Looking at the spectra in Figure 4b,c in comparison with the spectrum of the cells before inoculation in Figure 4a, it can be seen that both Bands 13 and 14 disappear at 48 hr from viral attack, while display weak at 72 hr. Also Bands 53 and 54 become weaker starting from 48 hr exposure to virus (cf. Figure 5a–c).

According to Mehraj and Routy (2015), infection triggers catabolism of tryptophan through the enzymatic activity of indoleamine-2,3-dioxygenase (IDO). IDO is an enzyme that exerts metabolic immune regulation by protecting the host cells from overreacting in their immune responses by means of induction to systemic immune tolerance. The main role in IDO is played by interferon-gamma, which acts as a catalyzer in the conversion of tryptophan into *N′*-formylkynurenine. As a consequence of increased IDO activity, tryptophan is gradually depleted from the host cell in response to viral attacks. Fox et al. (2013) specifically studied IDO in the context of influenza virus and reported that influenza infection promoted IDO activity in the lung parenchyma, with tryptophan being reduced to kynurenine and other metabolites. Figure 9b shows the structural rearrangement that reduces tryptophan to kynurenine upon enzymatic IDO reactions and the successive step of formylation to *N′*-formylkynurenine. The elimination of the indole ring clearly justifies the disappearance of its peculiar ring vibrations (i.e., Bands 13 and 14) in the Raman spectrum, as we have observed in Figure 4. Looking at additional details related to tryptophan in the Raman spectra before and after virus inoculation, Band 53 (at 1,348 cm^{-1}) represents a relatively strong signal, which arises from skeletal stretching in the six-membered benzene ring of tryptophan. This vibrational mode, also shown in Figure 9b, thus continues to occur independently of the disappearance of the five-membered pyrrole ring and of the catabolic reaction leading to *N′*-formylkynurenine. It remains conspicuously unchanged after virus inoculation, because scarcely affected by the IDO reduction of the indole ring (cf. Figures 5 and 9). Also Band 44 at 1,247 cm^{-1} remains conspicuously unaffected by IDO reduction. On the other hand, Band 69* newly appears at 1605, which is related to C–N stretching of the *N*-formyl group in *N′*-formylkynurenine (Bieker & Schmidt, 1979). As seen in Figure 9b, the formulation process leads to a new configuration of the C–N bond, which appears at a Raman frequency shifted by approximately 12 cm^{-1} toward higher wavenumbers with respect to triphosphate C═N stretching (Band 69 at 159 cm^{-1}; D'Amico et al., 2015; Madzharova et al., 2016). Concurrently, also a new frequency for Amide III vibrations appears (labeled as Band 44*) at 1239 cm^{-1}, which represents the new NH_2 configuration associated to the *N′*-formylkynurenine structure (cf. Figure 9b; Bieker & Schmidt, 1979). Note that also the reduction in strength after virus inoculation of Bands 29 (1,025 cm^{-1}) and 30 (1,035 cm^{-1}), both related to C–H bending in the benzene ring (Hernandez, Coic, Pfluger, Kruglik, & Ghomi, 2016; Hernandez, Pfluger, Kruglik, & Ghomi, 2013), could be explained as a consequence of the disappearance of the pyrrole ring upon formylation, according to a reduction in "stiffness" of the environment of the benzene ring following the dismantlement of the pyrrole ring. Figure 9c summarizes the spectroscopic fingerprints of IDO and formylation of the tryptophan structure that follow the inoculation of the Influenza A virus.

In summary, we propose here that a time-lapse Raman analysis as a function of virus inoculation time could enable one to trace in situ the path of IDO/formylation catabolic reactions of tryptophan, and thus to reveal the "efforts" of the MDCK cells in developing an antiviral reaction against the infectious agent. Our spectroscopic findings were found to be in agreement with a recent study by F. Li and Karlsson (2017). These researchers indeed reported that an upregulation of IDO, accompanied by degradation of tryptophan along the kynurenine pathway, contributed to limiting replication of Influenza A virus in the murine standard fibroblast cell line.

4.3 | Raman fingerprints of energy highjack machinery

In this section, we attempt to link the Raman spectra detected after viral inoculation with the machinery through which the Influenza A virus highjacks cells' energy. This process is based on adenosine dephosphorylation chemistry (Keck, Ataey, Amaya, Bailey, & Narayanan, 2015), according to which phosphate groups in the adenosine molecules detach to react with glycerol and form glycerol triphosphate. A confirmation for the process of consumption of adenosine triphosphate could be seen in the decrease of Band 52 (at 1,331 cm^{-1}), which is a strong signal in the Raman spectrum of adenosine triphosphate (D'Amico et al., 2015; Ochsenkühn, Jess, Stoquert, Dholakia, & Campbell, 2009), while Bands 16* and 19* (at ~816 and ~865 cm^{-1}, respectively), which belong to O–P–O stretching in adenosine monophosphate and in mono or diphosphate molecules, respectively, newly appear. While both vibrational frequencies at approximately 816 and 865 cm^{-1}, respectively, represent phosphate-stretching modes in adenosine biomolecules,

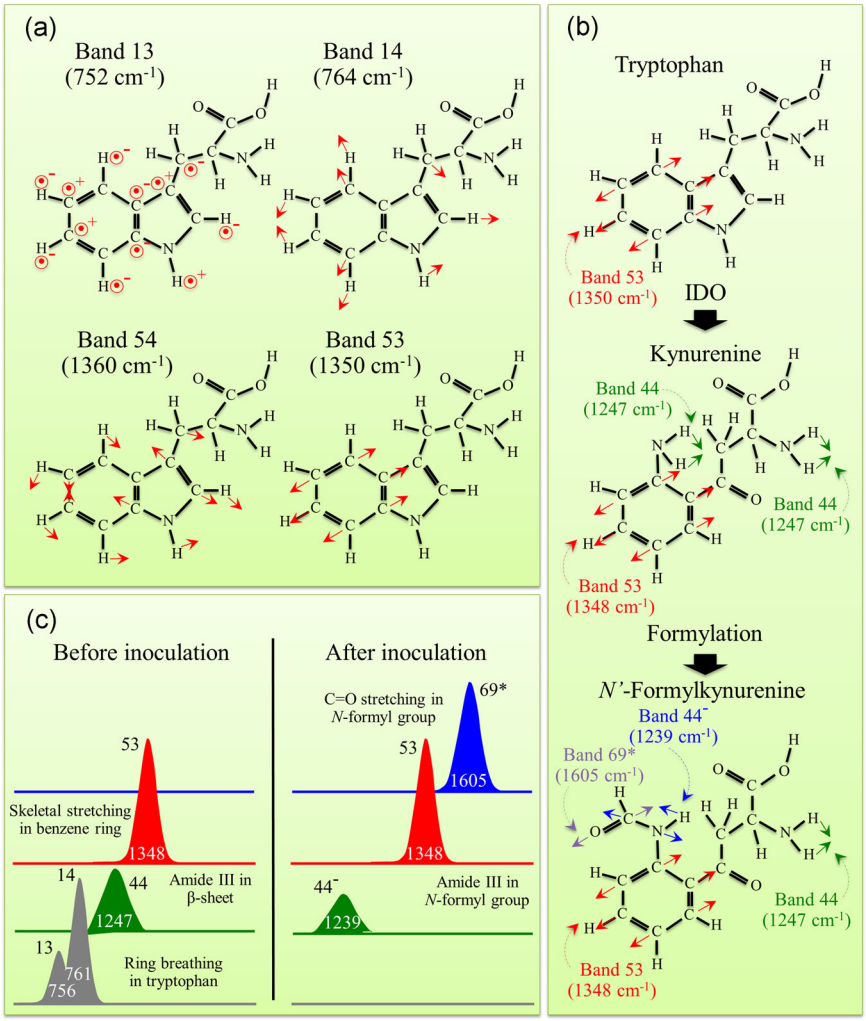

FIGURE 9 (a) Raman signals from tryptophan ring breathing and skeletal stretching, which correspond to Bands 13, 14, 53, and 54 (cf. Tables 1 and 2); (b) structural rearrangement after virus inoculation reduces tryptophan to kynurenine upon enzymatic IDO reactions and the successive step of formylation to *N′*-formylkynurenine; the indole ring disappears in the structure and so its peculiar ring breathing vibrations in the Raman spectrum (i.e., the three bands in (a)), skeletal stretching in the six-membered benzene ring (Band 53) and NH_2 bending (Band 44), which remain conspicuously unaffected, while "modified" Amide III vibrations newly appear (Bands 44*) after formylation; and, (c) summary of the spectroscopic fingerprints of IDO and formylation of the tryptophan structure following Influenza A virus inoculation

the first band is only peculiar to adenosine monophosphate, while the second one can be found in both mono and diphosphate molecules (Rimai et al., 1969). The observed intensity changes in O-P-O vibrational modes could be related to the process of hydrolysis (Bhaumik et al., 2014). Basic studies have demonstrated that Raman emissions from adenosine triphosphate, which typically occur in the spectral interval between 810 and 880 cm^{-1}, are enhanced at frequencies close to those of Bands 16* and 19* upon lowering environmental pH (Rimai et al., 1969). The relatively high initial intensity of Band 19 (at 852 cm^{-1}) is a cumulative contribution of O-P-O stretching in adenosine triphosphate and out-of-plane ring modes in tyrosine (H. M. Li et al., 1992; Yu et al., 1973). However, the decreasing trend observed for Band 19 after virus inoculation, which matches the above-mentioned one of Band 52 (Figure 4c,d), suggests a non-negligible contribution of O–P–O stretching in adenosine triphosphate to Band 19 according to Rimai et al. (1969), and supports the thesis of a dephosphorylation mechanism. Bands 16* and 19* instead represent diphosphate and monophosphate species originated from dephosphorylation of adenine triphosphate. Both bands appear after 48 hr inoculation at the expenses of the original Band 19 (cf. Figure 4c). The balance among hydrolysis products is then partly restored after 72 hr of viral inoculation (Figure 4(d)).

Single-stranded RNA influenza viruses might use different strategies to initiate and to control their replication through the synthesis of replicative intermediates (Deng, Vreede, & Brownlee, 2006). Adenosine hydrolysis is also required for virus budding (Hui & Nayak, 2001), and adenosine monophosphate was found to substitute for adenosine triphosphate in reactions catalyzed by RNA polymerase complexes to conveniently promote replication initiation (Deng, Sharp, & Brownlee, 2006). The free energy made available upon dephosphorylation of adenosine triphosphate (spontaneous reaction) allows the nonspontaneous formation of glycerol triphosphate needed for the formation of additional membrane phospholipids (Casiday, Herman, & Frey, 2018). Accordingly, three main chemical reactions can be drawn, which represent the energy machinery adopted by Influenza A virus to progress its viral multiplication, as follows (Kammermeier, 1998):

$$\text{Glycerol} + HPO_4^{2-} \rightarrow (\text{Glycerol} - 3 - \text{phosphate})^{2-} + H_2O \quad (1)$$

(Free energy = +9.2 kJ; non-spontaneous)

$$ATP^{4-} + H_2O \rightarrow ADP^{3-} + HPO_4^{2-} + H^+ \quad (2)$$

(Free energy = −30.5 kJ; spontaneous)

$$\text{Glycerol} + \text{ATP}^{4-} \rightarrow \left(\text{Glycerol}-3-\text{phosphate}\right)^{2-} + \text{ADP}^{3-} + \text{H}^{+} \quad (3)$$

(Free energy = −21.3 kJ; spontaneous)

where the abbreviations ATP and ADP refer to adenosine tri- and diphosphate, respectively. Spontaneously occurring Equations (2) and (3), which represent the process of dephosphorylation of adenosine, release a large amount of free energy. Such a free-energy availability in turn drives the non-spontaneous reaction of phosphorylation of glycerol molecules (Equation (1), which is a necessary step in the formation of new phospholipids for membrane buildup (formed by glycerol with a phosphate group and two fatty acid chains attached). In the Raman spectra after inoculation, one can indeed find an initial increase in the glycerol Band 2+ after 48 hr. A schematic draft of the overall biochemical process is given in Figure 10a.

To validate the thesis of adenosine dephosphorylation, one needs to monitor the development of the lipid species in the Raman spectrum after viral inoculation. An additional new band, labeled Band 15*, appears in the spectrum (Figure 4d) at around 789 cm^{-1} as a high-frequency shoulder to the DNA phosphodiester stretching Band 15. Band 15* belongs to O–P–O stretching in phosphatidylserine (Krafft et al., 2005). Note also that Band 15 (at 779 cm^{-1}), which is also contributed by phosphatidylinositol (Krafft et al., 2005), dramatically increase after 48 hr since inoculation (cf. Figure 4c). Viruses target lipid signaling, synthesis, and metabolism to remodel the host cells into a suitable environment for their replication (Heaton & Randall, 2011). Since specific viral processes require specific lipid compositions to allow suitable membrane composition and dynamics, the lipid microenvironment is key in viral contamination. Phosphatidylinositol kinase signaling is exploited by many viruses for reaching internalization (Liu et al., 2001), which explains the initial enhancement in the intensity of Band 15 observed for the inoculated cells (cf. Figure 4c). Regarding the enrichment in phosphatidylserine seen as the new Band 15* in cells inoculated for 48 hr, it was reported that some viruses enrich their membrane with this phospholipids for the macropinocytic clearance of apoptotic debris (Henson et al., 2001; Hoffmann et al., 2001; Small & Peticolas, 1971). It also mediated phagocytosis of Influenza A Virus-infected apoptotic HeLa cells

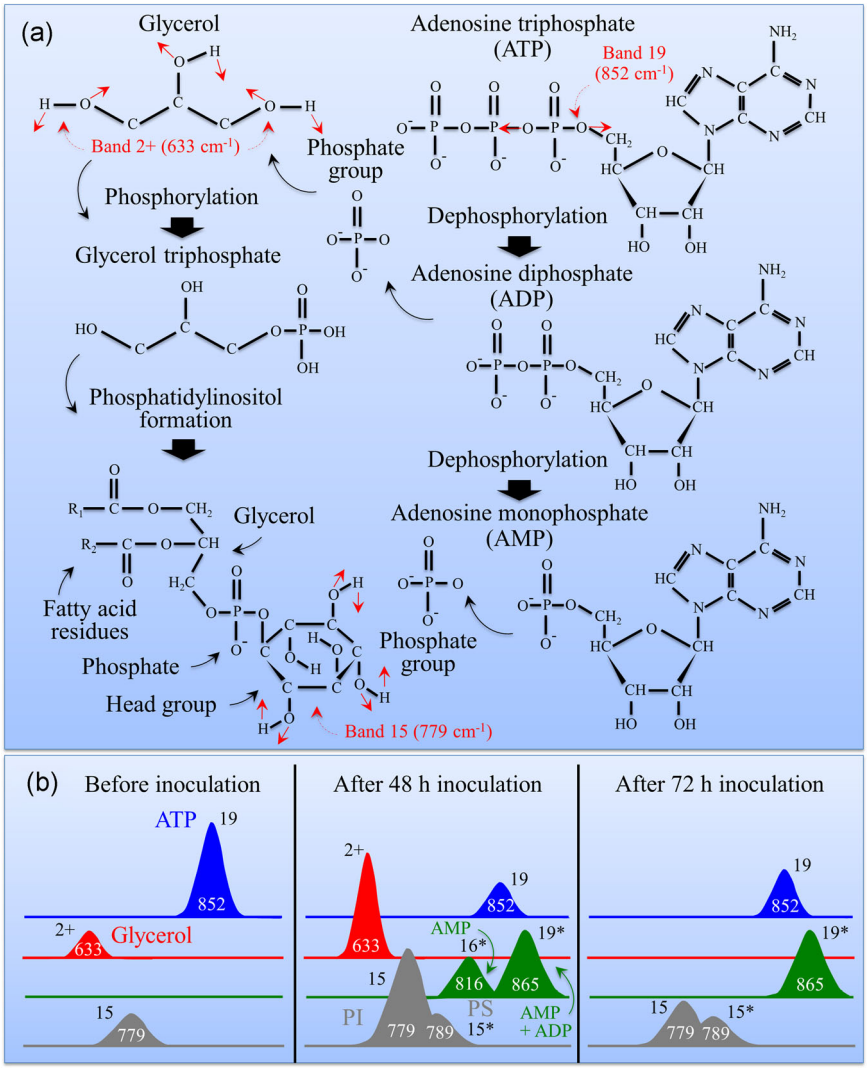

FIGURE 10 (a) Biochemical process of dephosphorylation of adenosine triphosphate (ATP) to form di- and monophosphates followed by phosphorylation of glycerol molecules and formation of phosphatidylinositol (PI) for membrane buildup (the main fingerprint vibrations are shown and labeled in inset); and, (b) summary of the spectroscopic fingerprints of dephosphorylation in adenosine triphosphate-driven formation of new lipid molecules, which follows Influenza A virus inoculation. Note that in (a) the C–O–H out-of-plane bending vibrations in the phosphatidylinositol ring are only shown on three sites for graphical reasons, but they refer to all five sites of the ring. The labels R_1 and R_2 refer to fatty acid residues and PS to phosphatidylserine

(Shiratsuchi et al., 2000). Accordingly, we can interpret the presence of the new Band 15* in the inoculated MDCK cells as part of the machinery involved with apoptosing cells, which expose phosphatidylserine as a phagocytic marker on their surfaces for phagocytes to recognize it and to engulf the marked cells (Ren & Savill, 1998; Savill et al., 1993). The Raman observation of lipid rearrangement might support the hypothesis that virus uses phosphatidylinositol in signaling while reaching internalization (Liu et al., 2001), which is also seen in the intensity increase of the additional phosphatidylinositol Band 34 (at 1,100 cm^{-1}; Krafft et al., 2005) after 72 hr; cf. Figure 5d). Note also that a number of dynamic processes of recruitment, activation or extraction of proteins from membranes are associated with specifically phosphorylated derivatives of phosphatidylinositol, referred to as phosphoinositides. In trafficking events, viruses use such chemical species, which provide reversible docking sites for regulatory factors through binding to the cytosolic side of membranes via esterified fatty acids, during infection (Vale-Costa & Amorim, 2016). The rationale for phosphatidylserine enrichment resides in the virus need for macropinocytic clearance of apoptotic debris (Henson et al., 2001; Hoffmann et al., 2001; Ren & Savill, 1998; Savill et al., 1993; Shiratsuchi et al., 2000). Figure 10b summarizes the spectral variations related to adenosine dephosphorylation and to the alterations in lipid composition that take place after viral inoculation.

Finally, a literature search showed that the energy highjack machinery is not a peculiarity of the Influenza A virus. Bardeletti (1977) reported that the quantity of cell adenosine triphosphate rapidly diminished in baby hamster kidney fibroblasts upon inoculation of the rubella virus (90 min after the infection the triphosphate level was 35% less than that of the control cells). In substance, the main biochemical phenomenon of energy transformation in the viral attack, which involves consumption of triphosphates to increase selected lipid contents, seems to be traceable in the Raman spectrum upon time-lapse monitoring the trends of specific fingerprint bands.

5 | CONCLUSION

In this study, we first separately examined Raman spectra collected on Influenza A virus and MDCK cells. The retrieved spectra greatly differed to each other because reflecting the very different biomolecular structures of the observed samples. Upon carrying out a comparison between virus and cell spectra, we assigned the observed bands to DNA, RNA, lipid, sugar alcohol, and protein molecules as their major constituents. We accurately labeled all the Raman emissions with high spectral resolution. Then, we recorded in situ Raman spectra in time-lapse fashion after virus inoculation into cells. In this latter analysis, we looked for molecular fingerprints of peculiar metabolic effects induced by the Influenza A virus to promote their own replication. Three fundamental biochemical phenomena were traced in the spectra and discussed, as follows:

(i) Viral obstruction to cell metabolism and unfolding of hemagglutinin when translated from the external viral envelope into a constrained endosomal volume (enzymatic hydrolysis).
(ii) The path of IDO/formylation catabolic reactions of tryptophan as a marker of the status of disease tolerance enforced by the MDCK cells in response to the viral agent.
(iii) The energetics machinery through which Influenza A virus retrieves free energy according to adenosine dephosphorylation chemistry to synthesize suitable lipid molecules.

The Raman procedures discussed here required high spectral resolution and deconvolution algorithms but did not involve staining, tagging or other manipulations incompatible with life. Although in this paper we only scratched the surface of the complex virus/cell biochemical interactions, the shown spectroscopic findings clearly uncovered a huge potential for future biophysics research using Raman spectroscopy.

ACKNOWLEDGMENTS

This work was supported by MEXT KAKENHI (No 17K01389).

CONFLICT OF INTERESTS

The authors declare that there are no conflict of interests.

AUTHOR CONTRIBUTIONS

G. P. designed the logic and wrote the paper, prepared the figures, set the chemical equations, and implemented the results and discussion. W. Z. provided labeling of the Raman spectra and discussed the vibrational issues. T. A. supervised cell cultures experiments. S. H. did the cell cultures and part of Raman experiments. E. M. contributed to the Raman results, interpretations and discussion. F. B. made Raman experiments and analyzed the results. E. O. supervised cell cultures, the inoculation, and collected fluorescence images. O. M. who is the immunologist of the group, provided the biological interpretation of the observed phenomena.

ORCID

Giuseppe Pezzotti http://orcid.org/0000-0002-9663-2429

REFERENCES

Baena, J. R., & Lendl, B. B. (2004). Raman spectroscopy in chemical bioanalysis. *Current Opinion in Chemical Biology*, *8*, 534–539.

Bankapur, A., Krishnamurthy, R. S., Zachariah, E., Santhosh, C., Chougule, B., Praveen, B., … Mathur, D. (2012). Micro-Raman spectroscopy of silver nanoparticle induced stress on optically-trapped stem cells. *PLOS One*, *7*, e35075.

Bardeletti, G. (1977). Respiration and ATP level in BHK21/13S cells during the earliest stages of Rubella virus replication. *Intervirol*, *8*, 100–109.

Bhaumik, A., Shearin, A. M., Delong, R., Wanekaya, A., & Ghosh, K. (2014). Probing the interaction at the nano-bio interface using Raman spectroscopy: ZnO nanoparticles and adenosine triphosphate biomolecules. *Journal of Physical Chemistry C*, *118*, 18631–18639.

Bieker, L., & Schmidt, H. (1979). Raman spectra of *N*-formylkynurenine derivatives of lysozyme produced by ozone oxidation. *FEBS Letters*, *106*, 268–270.

Bouvier, N. M., & Palese, P. (2008). The biology of influenza viruses. *Vaccine*, *26*(Suppl. 4), D-49–D-53.

Bradley, K. C., Galloway, S. E., Lasanajak, Y., Song, X., Heimburg-Molinaro, J., Yu, H., … Steinhauer, D. A. (2001). Analysis of influenza virus hemagglutinin receptor binding mutants with limited receptor recognition properties and conditional replication characteristics. *Journal of Virology*, *85*, 12387–12398.

Buehler, J., Navi, D., Lorusso, A., Vincent, A., Lager, K., & Miller, C. L. (2013). Influenza A virus PB1-F2 protein expression is regulated in a strain-specific manner by sequences located downstream of the PB1-F2 initiation codon. *Journal of Virology*, *87*, 10687–10699.

Cao, A., Liquier, J., & Taillandier, E. (1995). Infrared and Raman spectroscopy of biomolecules. In B.Schrader (Ed.), *Infrared and Raman Spectroscopy: Methods and Applications* (pp. 344–371). Cambridge, UK: VCH.

Carey, P. R. (1982). *Biochemical Applications of Raman and Resonance Raman Spectroscopies* (p. 89). New York, NY: Academic Press.

Casiday, R., Herman, C., & Frey, R. (2018). *Energy for the body: oxidative phosphorylation*. Retrieved from http://www.chemistry.wustl.edu/~edudev/LabTutorials/Cytochromes/cytochromes.html

Chan, J. W., Taylor, D. S., Zwerdling, T., Lane, S. M., Ihara, K., & Huser, T. (2006). Micro-Raman spectroscopy detects individual neoplastic and normal hematopoietic cells. *Biophysical Journal*, *90*, 648–656.

Chu, C. M., Dawson, I. M., & Elford, W. J. (1949). Filamentous forms associated with newly isolated influenza virus. *Lancet*, *1*, 602.

Chutiwitoonchai, N., & Aida, Y. (2016). NXT1, a novel Influenza A NP binding protein, promotes the nuclear export of NP via a CRM1-dependent pathway. *Viruses*, *8*, 209.

Combs, A., McCann, K., Autrey, D., Laane, J., Overman, S. A., & Thomas, G. J., Jr. (2005). Raman signature of the non-hydrogen-bonded tryptophan side chain in proteins: Experimental and ab initio spectra of 3-methylindole in the gas phase. *Journal of Molecular Structure*, *735-736*, 271–278.

Cordero, D., Lopez-Alvarez, M., Rodriguez-Valencia, C., Serra, J., Chiussi, S., & Gonzales, P. (2013). In vitro response of pre-osteoblastic cells to laser microgrooved PEEK. *Biomedical Materials*, *8*, 055006. (8 pages).

Cory, J. (2006). Purine and pyrimidine nucleotide metabolism. In T.Devlin (Ed.), *Textbook of biochemistry with clinical correlations* (6th ed., pp. 789–822). Hoboken, NJ: Wiley-Liss.

Cowcher, D. P., Deckert-Gaudig, T., Brewster, V. L., Ashton, L., Deckert, V., & Goodacre, R. (2016). Detection of protein glycosylation using tip-enhanced Raman scattering. *Analytical Chemistry*, *88*, 2105–2112.

D'Amico, F., Cammisuli, F., Addobbati, R., Rizzardi, C., Gessini, A., Masciovecchio, C., … Pascolo, L. (2015). Oxidative damage in DNA bases revealed by UV resonant Raman spectroscopy. *Analyst*, *140*, 1477–1485.

Novel Swine-Origin Influenza A (H1N1) Virus Investigation Team (SOIA Novel), Dawood, F. S., Jain, S., Finelli, L., Shaw, M. W., Lindstrom, S., … Uyeki, T. M. (2009). Emergence of a novel swine-origin influenza A (H1N1) virus in humans. *New England Journal of Medicine*, *360*, 2605–2615.

De Gelder, J., De Gussem, K., Vandenabeele, P., & Moens, L. (2007). Reference database of Raman spectra of biological molecules. *Journal of Raman Spectroscopy*, *38*, 1133–1147.

De Jesus, A. J., & Allen, T. W. (2013). The role of tryptophan side chains in membrane protein anchoring and hydrophobic mismatch. *Biochimica et Biophysica Acta, Biomembranes*, *1828*, 864–876.

Deng, T., Sharps, J. L., & Brownlee, G. G. (2006). Role of the influenza virus heterotrimeric RNA polymerase complex in the initiation and replication. *Journal of General Virology*, *87*, 3373–3377.

Deng, T., Vreede, F. T., & Brownlee, G. G. (2006). Different de novo initiation strategies are used by influenza virus RNA polymerase on its cRNA and viral RNA promoters during viral RNA replication. *Journal of Virology*, *80*, 2337–2348.

Dovbeshko, G. I., Chegel, V. I., Gridina, N. Y., Repnytska, O. P., Shirshov, Y. M., Tryndiak, V. P., … Solyanik, G. I. (2002). Surface enhanced IR absorption of nucleic acids from tumor cells: FTIR reflectance study. *Biopolym*, *67*, 470–486.

Ebner, S., & Marin-Grez, M. (1998). Video-imaging microfluorometry identifies alpha- and beta-like cell types in Madin-Darby canine kidney monolayers. *Kidney International*, *67*(Suppl.), S139–S142.

Eierhoff, T., Hrincius, E. R., Rescher, U., Ludwig, S., & Ehrhardt, C. (2010). The epidermal growth factor receptor (EGFR) promotes uptake of Influenza A viruses (IAV) into host cells. *PLoS Pathogens*, *6*):e1001099.

Faolain, E. O., Hunter, M. B., Byrne, J. M., Kelehan, P., McNamer, M., Byrne, H. J., & Lyng, F. M. (2005). A study examining the effects of tissue processing on human tissue sections using vibrational spectroscopy. *Vibr. Spectrosc*, *38*, 121–127.

Fernandez, R., Oliveira-Souza, M., & Malnic, G. (2000). Na^+-independent proton secretion in MDCK-C11 cells. *Pflugers Archiv. European Journal of Physiology*, *441*, 287–293.

Fox, J. M., Sage, L. K., Huang, L., Barber, J., Klonowski, K. D., Mellor, A. L., … Tripp, R. A. (2013). Inhibition of indoleamine 2,3-dioxygenase enhances the T-cell response to influenza virus infection. *Journal of General Virology*, *94*, 1451–1461.

Gambaryan, A. S., Karasin, A. I., Tuzikov, A. B., Chinarev, A. A., Pazynina, G. V., Bovin, N. V., … Olsen, C. W. (2005). A.I. Klimov, Receptor-binding properties of swine influenza viruses isolated and propagated in MDCK cells. *Virus Research*, *114*, 15–22.

Gekle, M., Wunsch, S., Oberleithner, H., & Silbernagl, S. (1994). Characterization of two MDCK-cell subtypes as a model system to study principal cell and intercalated cell properties. *Pflugers Archiv. European Journal of Physiology*, *428*, 157–162.

Gonchukov, S., Sukhinina, A., Bakhmutov, D., & Minaeva, S. S. (2012). Raman spectroscopy of saliva as a perspective method for periodontitis diagnostics. *Laser Physics Letters*, *9*, 73–77.

Heaton, N. S., & Randall, G. (2011). Multifaceted roles for lipids in viral infection. *Trends in Microbiology*, *19*, 368–375.

Henson, P. M., Bratton, D. L., & Fadok, V. A. (2001). Apoptotic cell removal. *Current Biology*, *11*, R795–R805.

Hernandez, B., Pfluger, F., Kruglik, S. G., & Ghomi, M. (2013). Characteristic Raman lines of phenylalanine analyzed by a multi-conformational approach. *Journal of Raman Spectroscopy*, *44*, 827–833.

Hernandez, B., Coic, Y. M., Pfluger, F., Kruglik, S. G., & Ghomi, M. (2016). All characteristic Raman markers of tyrosine and tyrosinate originate from phenol ring fundamental vibrations. *Journal of Raman Spectroscopy*, *47*, 210–220.

Hobro, A. J., Rouhi, M., Blanch, E. W., & Conn, G. L. (2007). Raman and Raman optical activity (ROA) analysis of RNA structural motifsin Domain I of the EMCV IRES. *Nucl. Acids Res*, *35*, 1169–1177.

Hoffmann, P. R., deCathelineau, A. M., Ogden, C. A., Leverrier, Y., Bratton, D. L., Daleke, D. L., … Henson, P. M. (2001). Phosphatidylserine (PS) induces PS receptor-mediated macropinocytosis and promotes clearance of apoptotic cells. *Journal of Cell Biology*, *155*, 649–659.

Huang, Z., McWilliams, A., Lui, M., McLean, D. I., Lam, S., & Zeng, H. (2003). Near-infrared Raman spectroscopy for optical diagnosis of lung cancer. *International Journal of Cancer*, *107*, 1047–1052.

Hui, E. K. W., & Nayak, D. P. (2001). Role of ATP in Influenza virus budding. *Virol*, *290*, 329–341.

Iconomidou, V. A., Chryssikos, G. D., Gionis, V., Willis, J. H., & Hamodrakas, S. J. (2001). "Soft"-cuticle protein secondary structure as revealed by FT-Raman, ATR FT-IR and CD spectroscopy. *Insect Biochemistry and Molecular Biology*, *31*, 877–855.

Jenkins, R. H., Tuma, R., Juuti, J. T., Bamford, D. H., & Thomas, G. J., Jr. (1999). A novel Raman spectrophotometric method for quantitative measurement of nucleoside triphosphate hydrolysis. *Biospectrosc*, *5*, 3–8.

Jess, P. R. T., Garces-Chavez, V., Riches, A. C., Herrington, C. S., & Dholakia, K. (2007). Simultaneous Raman micro-spectroscopy of optically trapped and stacked cells. *Journal of Raman Spectroscopy*, *38*, 1082–1088.

Johnson, C. R., Ludwig, M., & Asher, S. A. (1986). Ultraviolet resonance Raman characterization of photochemical transients of phenol, tyrosine, and tryptophan. *Journal of the American Chemical Society*, *108*, 905–912.

Kammermeier, H. (1998). Phosphorylation potential and free energy of ATP. *Advances in Organ Biology*, *4*, 159–169.

Kateinen, E., Elomaa, M., Laakkonen, U. M., Sippola, E., Niemela, P., Suhonen, J., & Jarninen, K. (2007). Qualification of the amphetamine content in seized street samples by Raman spectroscopy. *Journal of Forensic Sciences*, *52*, 88–92.

Keck, F., Ataey, P., Amaya, M., Bailey, C., & Narayanan, A. (2015). Phosphorylation of single stranded RNA virus proteins and potential for novel therapeutic strategies. *Viruses*, *7*, 5257–5273.

Keil, W., Geyer, R., Niemann, H., Dabrowski, J., & Klenk, H. D. (1984). The carbohydrates of the hemagglutinin of influenza virus. In R. W.Compans, & D. H. L.Bishop (Eds.), *Segmented Negative Strand Viruses* (pp. 289–298). San Francisco, CA: Academic Press, Inc.

Kline, N. J., & Treado, P. J. (1997). Raman chemical imaging of breast tissue. *Journal of Raman Spectroscopy*, *28*, 119–124.

Kolijenovic, S., Scut, T. B., Vincent, A., Kros, J. M., & Puppels, G. J. (2005). Detection of meningioma in dura mater by Raman spectroscopy. *Analytical Chemistry*, *77*, 7958–7965.

Krafft, C., Neudert, L., Simat, T., & Salzer, R. (2005). Near infrared Raman spectra of human brain lipids. *Spectrochim. Acta Part A*, *61*, 1529–1535.

Lakshimi, R. J., Kartha, V. B., Krishna, C. M., Solomon, J. G. R., Ullas, G., & Uma Devi, P. (2002). Tissue Raman spectroscopy for the study of radiation damage: Brain irradiation of mice. *Radiation Res*, *157*, 175–182.

Lambert, P. J., Whitman, A. G., Dyson, O. F., & Akula, S. M. (2006). Raman spectroscopy: The gateway into tomorrow's virology. *Virology Journal*, *3*, 51.

Lau, D. P., Huang, Z., Lui, H., Man, C. S., Berean, K., Morrison, M. D., & Zeng, H. (2003). Raman spectroscopy for optical diagnosis in normal and cancerous tissue of the nasopharynx - Preliminary findings. *Lasers in Surgery and Medicine*, *32*, 210–214.

Lazar, G. (2011). Influence of the substrate-electrode applied bias voltage on the properties of sputtered a-C:H thin films. *Journal of Physics: Condensed Matter*, *13*, 3011.

Li, F., & Karlsson, H. (2017). Antiviral effect of IDO in mouse fibroblast cells during influenza virus infection. *Viral Immunology*, *30*, 542–544.

Li, H. M., Wurrey, C. J., & Thomas, G. J., Jr. (1992). Structural studies of viruses by laser Raman spectroscopy. Part XXXVI. Cysteine conformation and sulfhydryl interactions in proteins and viruses. 2. Normal coordinate analysis of the cysteine side-chain in model compounds. *Journal of the American Chemical Society*, *114*, 7463–7469.

Li, M., Romero-Gonzales, M., Banwart, S. A., & Huang, W. E. (2012). Single cell Raman spectroscopy for cell sorting and imaging. *Current Opinion in Biotechnology*, *23*, 56–63.

Liu, K. Z., Jia, L., Kelsey, S. M., Newland, A. C., & Mantsch, H. H. (2001). Quantitative determination of apoptosis on leukemia cells by infrared spectroscopy. *Apoptosis*, *6*, 269–278.

Lopes, R. P., Marques, M. P. M., Valero, R., Tomkinson, J., & Batista de Carvalho, L. A. E. (2012). Guanine: A combined study using vibrational spectroscopy and theoretical methods. *Spectroscopy: An International Journal*, *27*, 273–292.

Lord, R. C., & Yu, N. T. (1970). Laser-Raman spectroscopy of biomolecules (I): Native lysozyme and its constituent amino acids. *Journal of Molecular Biology*, *50*, 509–524.

Lorenz, B., Wichmann, C., Stockel, S., Rosch, P., & Popp, J. (2017). Cultivation-free Raman spectroscopic investigations of bacteria. *Trends in Microbiology*, *25*, 413–424.

Lu, X., Liu, Q., Benavides-Montano, J. A., Nicola, A. V., Aston, D. E., Rasco, B. A., & Aguilar, H. C. (2013). Detection of receptor-induced glycoprotein conformational changes on enveloped virions by using confocal micro-Raman spectroscopy. *Journal of Virology*, *87*, 3130–3142.

Lugovtsev, V. Y., Melnyk, D., & Weir, J. P. (2013). Heterogeneity of the MDCK cell line and its applicability for Influenza virus research. *PLOS One*, *8*, e75014.

Lynch, J. P., III, & Walsh, E. E. (2007). Influenza: Evolving strategies in treatment and prevention. *Seminars in Respiratory and Critical Care Medicine*, *28*, 144–158.

Madzharova, F., Heiner, Z., Guhlke, M., & Kneipp, J. (2016). Surface-enhanced hyper-Raman spectra of adenine, guanine, cytosine, thymine, and uracil. *Journal of Physical Chemistry C*, *120*, 15415–15423.

Maines, T. R., Jayaraman, A., Belser, J. A., Wadford, D. A., Pappas, C., Zeng, H., … Tumpey, T. M. (2009). Transmission and pathogenesis of swine-origin 2009 A(H1N1) influenza viruses in ferrets and mice. *Science*, *325*, 484–487.

Malini, R., Venkatakrishma, K., Kurien, J., Pai, K. M., Rao, L., Kartha, V. B., & Krishna, C. M. (2006). Discrimination of normal, inflammatory, premalignant, and malignant oral tissue: A Raman spectroscopy study. *Biopolym*, *81*, 179–193.

Mehraj, V., & Routy, J. P. (2015). Tryptophan catabolism in chronic viral infections: Handling uninvited guests. *International Journal of Tryptophan Research: IJTR*, *8*, 41–48.

Mellor, A. L., & Munn, D. H. (2003). Tryptophan catabolism and regulation of adaptive immunity. *Journal of Immunology*, *170*, 5809–5813.

Movasaghi, Z., Rehman, S., & Rehman, I. U. (2007). Raman spectroscopy of biological tissues. *Applied Spectroscopy Reviews*, *42*, 493–541.

Muramoto, Y., Noda, T., Kawakami, E., Akkina, R., & Kawaoka, Y. (2013). Identification of novel Influenza A virus proteins translated from PA mRNA. *Journal of Virology*, *87*, 2455–2462.

Nishimura, Y. (1985). Sequence dependent DNA conformations: Raman spectroscopic studies and a model of action of restriction enzymes. *Advances in Biophysics*, *20*, 59–74.

Nogales, A., Baker, S. F., Ortiz-Riano, E., Dewhurst, S., Topham, D. J., & Martinez-Sobrido, L. (2014). Influenza A virus attenuation by codon deoptimization of the NS gene for vaccine development. *Journal of Virology*, *88*, 10525–10540.

Notingher, I. (2007). Raman spectroscopy cell-based biosensors. *Sensors*, *7*, 1343–1358.

Notingher, I., & Hench, L. L. (2006). Raman microspectroscopy: A noninvasive tool for studies of individual living cells *in vitro*. *Expert Rev. Med. Dev. 3*, 215–234.

Notingher, I., Verrier, S., Haque, S., Polak, J. M., & Hench, L. L. (2003). Spectroscopic study of human lung epithelial cells (A549) in culture: Living cells versus dead cells. *Biopolym*, *72*, 230–240.

Novelli-Rousseau, A., Espagnon, I., Filiputti, D., Gal, O., Douet, A., Mallard, F., & Josso, Q. (2018). Culture-free antibiotic-susceptibility determination from single-bacterium Raman spectra. *Scientific Reports*, *8*, 3957.

Ochsenkühn, M. A., Jess, P. R. T., Stoquert, H., Dholakia, K., & Campbell, C. J. (2009). Nanoshells for surface-enhanced Raman spectroscopy in eukaryotic cells: Cellular response and sensor development. *ACS Nano*, *3*, 3613–3621.

Otange, B. O., Birech, Z., Okonda, J., & Rop (2017). Conductive silver paste smeared glass substrates for label-free Raman spectroscopic detection of HIV-1 and HIV-1 p24 antigen in blood plasma. *Analytical and Bioanalytical Chemistry*, *409*, 3253–3259.

Otto, C., van den Tweel, T. J. J., de Mul, F. F. M., & Greve, J. (1986). Surface-enhanced Raman spectroscopy of DNA bases. *Journal of Raman Spectroscopy*, *17*, 289–298.

Palese, P., & Shaw, M. L. (2007). Orthomyxoviridae: The viruses and their replication. In D. M.Knipe, & P. M.Howley (Eds.), *Fields Virology 5th*

Edition (pp. 1647–1689). Philadelphia, PA: Lippincott Williams & Wilkins.

Palese, P., Zheng, H., Engelhardt, O. G., Pleschka, S., & Garcia-Sastre, A. (1996). Negative-strand RNA viruses: Genetic engineering and applications. *Proceedings of the National Academy of Sciences USA*, *93*, 11354–11358.

Peticolas, W. L. (1995). Raman spectroscopy of DNA and proteins. *Methods in Enzymology*, *246*, 389–416.

Podstawka, E., Ozaki, Y., & Proniewicz, L. M. (2004). Part II: Surface-enhanced Raman spectroscopy investigation of methionine containing heterodipeptides adsorbed on colloid silver. *Applied Spectroscopy*, *58*, 581–590.

Prescott, B., Steinmetz, W., & Thomas, G. J., Jr. (1984). Characterization of DNA structures by laser Raman spectroscopy. *Biopolym*, *23*, 235–256.

Rabadan, R., Levine, A. J., & Robins, H. (2006). Comparison of avian and human Influenza A viruses reveals a mutational bias on the viral genomes. *Journal of Virology*, *80*, 11887–11891.

Ren, Y., & Savill, J. (1998). Apoptosis: The importance of being eaten. *Cell Death and Differentiation*, *5*, 563–568.

Rimai, L., Cole, T., Parsons, J. L., Hickmott, J. T., & Carew, E. B. (1969). Studies of Raman spectra of water solutions of adenosine tri-, di-, and monophosphate and some related compounds. *Biophysical Journal*, *9*, 320–329.

Ruokola, P., Dadu, E., Kazmertsuk, A., Hakkanen, H., Marjomaki, V., & Ihalainen, J. A. (2014). Raman spectroscopic signatures of Echovirus 1 uncoating. *Journal of Virology*, *88*, 8504–8513.

Salzwedel, K., West, J. T., & Hunter, E. (1999). A conserved tryptophan-rich motif in the membrane-proximal region of the human immunodeficiency virus type 1 gp41 ectodomain is important for env-mediated fusion and virus infectivity. *Journal of Virology*, *73*, 2469–2480.

Sanchez, E. L., & Lagunoff, M. (2015). Viral activation of cellular metabolism. *Virology*, *479-480*, 609–618.

Savill, J., Fadok, V., Henson, P., & Haslett, C. (1993). Phagocyte recognition of cells undergoing apoptosis. *Immunology Today*, *14*, 131–136.

Scheiffele, P., Roth, M. G., & Simons, K. (1997). Interaction of influenza virus haemagglutinin with sphingolipid-cholesterol membrane domains via its transmembrane domain. *EMBO Journal*, *16*, 5501–5508.

Schmidt, H., & Bieker, L. (1979). Raman spectra of chemically modified lysozyme. Oxindole derivatives. *Archives of Biochemistry and Biophysics*, *195*, 205–210.

Severcan, F., Akkas, S. B., Turker, S., & Yucel, R. (2012). Methodological approaches from experimental to computational analysis in vibrational spectroscopy and microspectroscopy. In Severcan, F., & Haris, P. I. (Eds.), *Vibrational Spectroscopy in Diagnosis and Screening* (pp. 12–52). Amsterdam, The Netherlands: IOS Press.

She, C. Y., Dinh, N. D., & Tu, A. T. (1974). Laser Raman scattering of glucosamine, N-acetylglucosamine, and glucuronin acid. *Biochimica et Biophysica Acta/General Subjects*, *372*, 345–357.

Shetty, G., Kendall, C., Shepherd, N., Stone, N., & Barr, H. (2006). Raman spectroscopy: Evaluation of biochemical changes in carcinogenesis of oesophagus. *British Journal of Cancer*, *94*, 1460–1464.

Shiratsuchi, A., Kaido, M., Takizawa, T., & Nakanishi, Y. (2000). Phosphatidylserine-mediated phagocytosis of Influenza A virus-infected cells by mouse peritoneal macrophages. *Journal of Virology*, *74*, 9240–9244.

Siamwiza, M. N., Lord, R. C., Chen, M. C., Takamatsu, T., Harada, I., Matsuura, H., & Shimanouchi, T. (1975). Interpretation of the doublet at 850 and 830 cm^{-1} in the Raman spectra of tyrosyl residues in proteins and certain model compounds. *Biochem*, *14*, 4870–4876.

Small, E. W., & Peticolas, W. L. (1971). Conformational dependence of Raman scattering intensities from polynucleotides. III. Order-disorder changes in helical structures. *Biopolym. 10*, 1377–1416.

Smith, E., & Dent, G.G. (2006). *Modern Raman Spectroscopy - A practical Approach*. John Wiley & Sons.

Smith, R., Wright, K. L., & Ashton, L. (2016). Raman spectroscopy: An evolving technique for live cell studies. *Analyst*, *141*, 3590–3600.

Stegmann, T., Booy, F. P., & Wilschut, J. (1987). Effects of low pH on influenza virus. *Journal of Biological Chemistry*, *262*, 17744–17749.

Stone, N., Kendall, C., Shepherd, N., Crow, P., & Barr, H. (2002). Near-infrared Raman spectroscopy for the classification of epithelial pre-cancers and cancers. *Journal of Raman Spectroscopy*, *33*, 564–573.

Stone, N., Kendall, C., Smith, J., Crow, P., & Barr, H. (2004). Raman spectroscopy for identification of epithelial cancers. *Faraday Discussion*, *126*, 141–157.

Strola, S. A., Baritaux, J. C., Schultz, E., Simon, A. C., Allier, C., Espagnon, I., … Dinten, J. M. (2014). Single bacteriaidentification by Raman spectroscopy. *Journal of Biomedical Optics*, *19*, 111610.

Sumayya, A., Panicker, C. Y., Tresa Varghese, H., & Harikumar, B. (2008). Vibrational spectroscopic studies and ab initio calculations of L-Glutamic acid 5-amide. *Rasayan Journal of Chemistry*, *1*, 548–555.

Takeuchi, H., & Harada, I. (1986). Normal coordinate analysis of the indole ring. *Spectrochimica Acta*, *42A*, 1069–1078.

Takeuchi, H., Nemoto, Y., & Harada, I. (1990). Environments and conformations of tryptophan side chains of gramicidin A in phospholipid bilayers studied by Raman spectroscopy. *Biochemistry*, *29*, 1572–1579.

Talari, A. C. S., Movasaghi, Z., & Rehman, I. (2015). Raman spectroscopy of biological tissues. *Applied Spectroscopy Reviews*, *50*, 46–111.

Tang, Y., Zaitseva, F., Lamb, R. A., & Pinto, L. H. (2002). The gate of the Influenza virus M2 proton channel is formed by a single tryptophan residue. *Journal of Biological Chemistry*, *277*, 39880–39886.

Te Velthuis, A. J. W., & Fodor, E. (2016). Influenza virus RNA polymerase: Insights into the mechanisms of viral RNA synthesis. *Nature Reviews Microbiology*, *14*, 479–493.

Teh, S. K., Zheng, W., Ho, K. Y., Teh, M., Yeoh, K. G., & Huang, Z. (2008). Diagnostic potential of near-infrared Raman spectroscopy in the stomach: Differentiating dysplasia from normal tissue. *British Journal of Cancer*, *98*, 457–465.

Thomas, G. J., Jr. (1976a). Raman spectroscopy of viruses and protein-nucleic acid interactions. *The SPEX Speaker*, *21*, 1–11.

Thomas, G. J., & Murphy, P., Jr. (1975). Structure of coat proteins in Pf1 and fd virions by laser Raman spectroscopy. *Science*, *188*, 1205–1207.

Thomas, G. J. Jr (1976b). Raman spectroscopy and virus research. *Applied Spectroscopy*, *30*, 483–494.

Tuma, R. (2005). Raman spectroscopy of proteins: From peptides to large assemblies. *Journal of Raman Spectroscopy*, *36*, 307–319.

Tuma, R., & Thomas, G. J. (2002). Raman spectroscopy of viruses. In Chalmers, J. M., & Griffiths, P. R. (Eds.), *Handbook of Vibrational Spectroscopy Vol. 5* (pp. 3515–3535). Chichester, UK: Wiley.

Vale-Costa, S., & Amorim, M. J. (2016). Recycling endosomes and viral infection. *Viruses*, *8*, 64. (29 pages).

Viehoever, A. R., Anderson, D., Jansen, D., & Mahadevan-Jansen, A. (2003). Organotypic raft cultures as an effective in vitro tool for understanding Raman spectral analysis of tissues. *Photochemistry and Photobiology*, *78*, 517–524.

Wang, Q., Lin, T., Johnson, J. E., & Finn, M. G. (2002). Natural supramolecular building blocks: Cysteine-added mutants of Cowpea mosaic virus. *Chemistry & Biology*, *9*, 813–819.

Williams, A. C., & Edwards, H. G. M. (1994). Fourier transform Raman spectroscopy of bacterial cell walls. *Journal of Raman Spectroscopy*, *25*, 673–677.

Wunsch, S., Gekle, M., Kersting, U., Schuricht, B., & Oberleithner, H. (1995). Phenotypically and karyotypically distinct Madin-Darby canine kidney cell clones respond differently to alkaline stress. *Journal of Cellular Physiology*, *164*, 164–171.

Xu, Y., & Lu, C. (2005). Raman spectroscopic study on structure of human immunodeficiency virus (HIV) and hypericin-induced photosensitive damage of HIV. *Science in China, Series C: Life Sciences*, *48*, 117–132.

Yang, H., Carney, P. J., Mishin, V. P., Guo, Z., Chang, J. C., Wentworth, D. E., … Stevens, J. (2016). Molecular characterizations of surface proteins hemagglutinin and neuraminidase from recent H5Nx avian Influenza viruses. *Journal of Virology*, *90*, 5770–5784.

Ye, S., Li, H., Yang, W., & Luo, Y. (2014). Accurate determination of interfacial protein secondary structure by combining interfacial-sensitive Amide I and Amide III spectral signals. *Journal of the American Chemical Society*, *136*, 1206–1209.

Yu, N. T., Jo, B. H., & O'Shea, D. C. (1973). Laser Raman scattering of cobramine B, a basic protein from cobra venom. *Archives of Biochemistry and Biophysics*, *156*, 71–76.

Zhang, Q., Andrew Chan, K. L., Zhang, G., Gillece, T., Senak, L., Moore, D. J., …Flach, C. R. (2011). Raman microspectroscopic and dynamic vapor sorption characterization of hydration in collagen and dermal tissue. *Biopolymers*, *95*, 607–615.

Zhu, G., Zhu, X., Fan, Q., & Wan, X. (2011). Raman spectra of amino acids and their aqueous solutions. *Spectrochimica Acta Part A*, *78*, 1187–1195.

How to cite this article: Pezzotti G, Zhu W, Adachi T, et al. Metabolic machinery encrypted in the Raman spectrum of influenza A virus-inoculated mammalian cells. *J Cell Physiol*. 2019;1–25. https://doi.org/10.1002/jcp.29392